



Characterization of wall filming and atomization inside a gas-turbine swirl injector

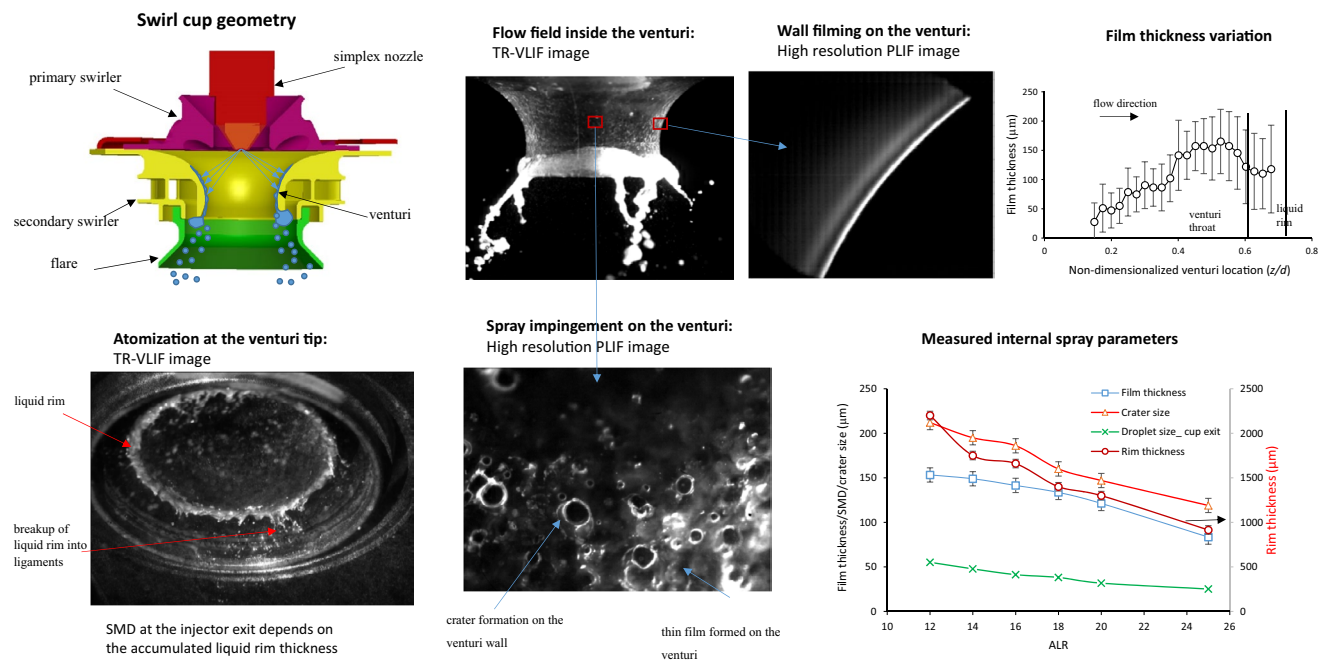
K. P. Shanmugasdas¹ · S. R. Chakravarthy¹ · R. Narasimha Chiranthan² · Jayanth Sekar² · Sundar Krishnaswami²

Received: 2 March 2018 / Revised: 13 August 2018 / Accepted: 30 August 2018 / Published online: 14 September 2018
© Springer-Verlag GmbH Germany, part of Springer Nature 2018

Abstract

The internal atomization characteristics of a practical gas turbine fuel injector are investigated comprehensively using various laser flow diagnostic techniques. The injector consists of a pilot spray surrounded by a primary swirl air, with the spray impinging on a venturi prefilmer to form a liquid film that accumulates into a rim at the venturi tip, which in turn is sheared by a counter-rotating secondary swirl air. The atomizer geometry is modularized into different configurations to access the internal flow field. The quantitative measurements made are with a phase Doppler interferometer at different stages of the injector and time-resolved volume or planar laser induced fluorescence (TR-V/PLIF) imaging. The different internal atomization characteristics such as the liquid film thickness variation, size distribution of craters formed by primary spray droplets impinging on the liquid film, rim thickness at the venturi tip, and droplet size and velocity distribution at different stages are measured. It is found that the film dynamics is influenced by the droplet splashing and the shearing action of the primary air. The liquid rim at the venturi tip is the major source of droplets at the injector exit rather than the liquid film. The unsteady evolution of the multiphase flow inside the injector is dictated by the precessing vortex core of the primary swirl. However, the atomization process is mainly influenced by the central toroidal recirculation zone of the primary swirl flow and the counter-rotating shear layer acting on the accumulated liquid rim at the venturi tip.

Graphical abstract



Extended author information available on the last page of the article

1 Introduction

Modern gas turbine combustors demand high combustion performance and operational efficiency, besides meeting stringent emission requirements. Even though a great deal of technological advances have been taking place in the evolution of engine combustors over the past 5 decades, one major area still requiring further attention is the fuel injection process. First, the reacting flow field in the primary zone of the combustor is determined by the fuel injector. Second, sufficient level of atomization and uniform droplet dispersion within the combustor are the important prerequisites to achieve stable and efficient combustion. The spatial and temporal variation of the fuel droplets inside the combustor governs the local equivalence ratio, controls the residence time of the fuel–air mixture, and affects the combustion efficiency and transient flame stability characteristics (ignition, blow off, and thermo-acoustic instabilities) (Lefebvre 1975).

Most of the aero engine combustors currently in service employ a prefilming type of airblast atomizers. Such atomizers exhibit superior capabilities in providing efficient atomization and uniform fuel air mixing over a wide range of stoichiometric conditions, with less soot and smoke emissions (Lefebvre 1980). Early investigations focused on the performance characteristics of different airblast atomizers (Aigner and Wittig 1988; Elshanawany and Lefebvre 1980; Lefebvre 1980; Rizk and Lefebvre 1980, 1983; Rizkalla and Lefebvre 1975; Sattelmayer and Wittig 1986). They have parametrically investigated the role of fluid properties, fuel and air mass flow rates, and geometrical features of the atomizer on the final drop size produced at the injector exit. These enormously elaborate that investigations have collectively enabled empirical correlations to be developed to predict the final drop size [Sauter mean diameter (SMD)] as a function of above parameters.

One of the major disadvantages with the prefilming-type atomizers mentioned above is the insufficient atomization at low power operating conditions because of low air velocity. To overcome this, current aero engines utilize high shear, variable fuel placement airblast atomizers to expand the operational range and stability limits. One of the methods is to use a pilot injector (simplex or dual orifice type) to generate a primary spray that supplies droplets at low power conditions on the one hand. During high power conditions, on the other hand, majority of this spray is allowed to impinge on the prefilmer wall, which subsequently acts as a prefilming airblast atomizer. This concept is adopted in an atomizer called the “swirl cup”, which is employed in combustors of different aero engines (Mongia et al. 2001). Similarly, other designs adopt multiple co-flowing swirling airstreams with multiple fuel circuits within the injector (Brundish et al. 2003; Foust et al. 2012; Jasuja 2006).

These advanced fuel injectors produce a complex swirl flow field that affects the atomization characteristics. At high swirl number, the flow undergoes vortex breakdown, creating a central toroidal recirculation zone (CTRZ) at the atomizer exit. This aids in flame holding and creates a region of high turbulence that promotes rapid mixing and heat transfer (Gupta et al. 1984). Several investigators have reported the effect of swirl flow characteristics on airblast atomization (Gurubaran et al. 2008; Jeng et al. 2004; Lin et al. 2009; McDonnell et al. 1994; Wang et al. 1992). They have reported the dispersion of droplets into the CTRZ, depending on the droplet size, and the role of the CTRZ in enhancing atomization and mixing. Recently, Rajamanickam and Basu (2017a, b) reported different breakup modes and dispersion regimes of the droplets based on the local circulation strength and injection location within the swirl flow field. In the case of a simplex nozzle spray surrounded by a swirl flow field, the liquid sheet oscillations scaled up with the frequencies of the air phase KH instabilities waves (Rajamanickam and Basu 2017b).

The presence of a precessing vortex core (PVC) in turbulent swirl combustion devices is reported by a number of investigators (Syred 2006; Syred and Beer 1974; Wang et al. 1995), specifically in airblast sprays (Batarseh et al. 2009; Gepperth et al. 2010; Gurubaran et al. 2008; Mongia et al. 2001). The PVC can affect the instantaneous flow field as it displaces the vortex/spray core towards the chamber wall and increases the tangential velocity (Huang and Yang 2009). The spray precession at the injector exit is observed in some practical atomizers, which is influenced by the PVC (Gurubaran et al. 2008). Wang et al. (2007) performed large eddy simulations (LES) on the swirl cup and the characteristics of the CTRZ together with the PVC are captured in detail. The PVC is identified as the major mechanism that dictates the unsteady air flow evolution inside the swirl cup. Multiple swirling airstreams and their interaction with the ambient air lead to the shedding of large coherent structures at the injector exit (Lin et al. 2009). These temporal fluctuations in the flow lead to the formation of rich and lean fuel–air pockets that convect alternately (Schildmacher et al. 2000). Batarseh et al. (2009) measured the unsteady fluctuation frequencies in an airblast spray and proposed a scaling analysis to predict the spray frequencies. Local oscillations created by these instabilities, arising from the injector, can affect the combustor performance significantly. Thus, spatial or temporal instabilities arising from the injector can drastically alter the flow field and can affect the combustion efficiency and emissions (Gupta 1997).

Most of the investigations mentioned above have focused on the external spray characteristics and the role of the air-flow field on the atomization under different operating conditions. Even though this contributes to the understanding of the spray characteristics of these atomizers, the internal

multiphase flow features are not explored well so far. Therefore, a detailed quantitative understanding of the atomization process inside the fuel injector is essential to improve the design and performance capabilities of gas turbine combustors. However, this is scarcely available, mainly because of the complexities associated with accessing the atomizer geometry and flow field. Modern atomizer geometries consisting of multiple swirlers and prefilmer are complicated, which poses a major challenge for optical diagnostics.

The multiphase flow field inside the atomizer involves many physical processes. This includes the interaction of the simplex nozzle spray with the swirling primary air, droplet wall interactions, wall filming, atomization at the prefilmer tip in the presence of counter rotating air streams, and subsequent secondary atomization. Further, these processes occur in a small region inside the injector, and hence, diagnosing them altogether is practically difficult. This has prompted researchers to investigate one or two individual processes in relatively simplified geometries. The characteristics of spray impingement on a wall are reported in previous investigations (Roisman and Tropea 2002, 2005; Sivakumar and Tropea 2002). Incessant impingement of droplets from a spray on a wall wetted by a liquid film results in splashing and secondary drop formation, depending on the flow regimes. The film correspondingly thickens or thins alternately as the droplets impinge, splash, and/or merges with it. The characteristic velocity and size of the fluctuating liquid film are affected by the droplet impingement parameters and the film behaviour is characterized statistically. Batarseh (2008) investigated the spray–wall interaction with an inclined wall configuration and developed a model to predict the film thickness from the impingement parameters. In coaxial thin film flows, planar laser-induced fluorescence (PLIF) imaging is implemented to quantify the film thickness with high spatial and temporal resolution (Rodríguez and Shedd 2004; Schubring et al. 2010).

The film motion and liquid sheet breakup on a planar prefilming wall are investigated by Bhayaraju and Hassa (2009). The co-flowing air induces Kelvin–Helmholtz (K–H) instability on the liquid surface, which results in the formation of large amplitude surface waves. This film proceeds downstream and undergoes a wavy sheet breakup at the prefilmer tip. Inamura et al. (2012) reported that at the prefilmer tip, the liquid film undergoes a bag breakup into finer droplets, and the liquid rim breaks up into bigger ligaments. In the case of a planar prefilmer, Geppert et al. (2012) observed the thickness of the prefilmer tip and the air velocity as the most influential parameters governing the final droplet size, among other parameters such as the prefilmer length, liquid physical properties, and liquid flow rate. They observed that the mean frequency of ligament breakup from the rim is found to be inversely proportional to the prefilmer tip thickness. The effect of the prefilmer thickness on the ligament

size becomes more predominant when the thickness is $> 100 \mu\text{m}$ (Barun et al. 2015). Recently, we have conducted a detailed characterization of the two-phase flow inside a canonical geometry of a coaxial prefilming airblast atomizer (Shanmugadas and Chakravarthy 2017). The wall filming and ligament breakup process are characterized using LIF measurements and detailed statistics have been generated on film thickness, rim thickness, crater size, etc., along with correlations for the SMD.

Even though the above studies offer considerable insight into the different mechanisms involved in prefilming airblast atomization, they are insufficient to describe the complete sequence of all the processes governing the atomizer performance in a practical geometry. Further, for the design of advanced gas turbine atomizers, it is not possible to rely on the empirical correlations and models developed by the studies mentioned above, since their applicability is restricted to a particular, simple experimental configuration. Similarly, the applicability of the different models evolved from these studies to practical atomizers is not well proven so far. On the other hand, a complete computational fluid dynamics (CFD) simulation of the two-phase flow inside a practical atomizer is challenging and computationally expensive, and is also not fully successful as yet. Further, CFD models require input data from the real injector experiments for successful numerical simulation. The above factors emphasize the demand to carry on investigations on the wall filming and atomization process inside a practical airblast atomizer to understand various physical mechanisms in particular. Further, under realistic conditions, the atomization completes within a few mm from the atomizer exit. It is required to correlate the internal flow features to the final droplet size at the atomizer exit. The individual processes and the relative role of the atomizer components on the overall atomizer performance also need to be investigated. This will help to understand the flow physics better and also to develop full CFD model validations, so that design approach of atomizers is generalized and moves away from a geometry-specific empirical methodology.

In the present work, we present a comprehensive investigation on the evolution of the two-phase flow inside a practical fuel injector, namely, the swirl cup. A vast array of past studies already exists on the swirl cup (Cai et al. 2003; Hsiao and Mongia 2003; Jeng et al. 2004; Mongia et al. 2001; McDonnell et al. 1994; Wang et al. 1992, 1994, 2007). The solid model and cut section of the swirl cup assembly are shown in Fig. 1. Briefly, the geometry consists of a pair of counter-rotating primary and secondary air swirlers, and a liquid prefilming surface called the venturi in between the two air swirling stages. In a practical engine, the original equipment includes the swirl cup and a dual orifice nozzle as the pilot nozzle. The dual orifice nozzle forms a central spray with a narrow cone angle at low power operating

conditions and the secondary fuel circuit opens at higher power conditions, which causes much of the wall filming. The focus of the present work is on the wall filming aspect, but investigated at atmospheric pressure ambience. For the same range of air flow velocities and air-to-liquid ratio (ALR), the dual orifice nozzle is not suitable to obtain the wide cone angle of high power conditions at atmospheric ambient pressure. Thus, a simplex nozzle producing a 90° hollow cone spray is used as the pilot nozzle in the present work, similar to the previous investigations. This is suitable for the atmospheric ambient experiments in which majority of droplets impinge upon the venturi wall and results in a proper wall filming. Further work with the dual orifice nozzle under realistic engine operating conditions of high pressure and temperature of the ambient air is being performed at our laboratory, and will be reported in the future.

The working of the swirl cup with a simplex nozzle has been qualitatively understood based on works cited above and others on modelling (e.g., Mongia et al. 2001) as follows. The spray produced by the simplex nozzle is atomized by the swirling primary air. Under the influence of the primary swirler air, a majority of the simplex nozzle spray impinges on the venturi wall, forming a thin film. This film is sheared into finer droplets by the shear layer formed by the counter-rotating air flows at the venturi tip. The resulting spray issues out of the flare as a bell-shaped hollow cone spray with a recirculation zone at the centre.

In the present paper, the internal flow features of the swirl cup are investigated using different optical flow diagnostics techniques. This study is aimed to improve the understanding of the prefilming airblast atomization in practical atomizers, focusing on the film behaviour, spray-wall interaction, the ligament breakup process, etc. The atomization process inside the swirl cup is studied using a stage-wise phase Doppler interferometer (PDI) measurements and time-resolved imaging to understand the role of the individual components of the swirl cup towards improving the atomization. The wall filming and ligament breakup on the prefilmer wall are visualized using laser induced fluorescence (LIF) imaging experiments. Measurements are obtained to quantify the film thickness and the droplet impingement characteristics on the

prefilmer wall. It is intended to build up a detailed database of these internal atomization measurements, which can be employed for CFD validation and to develop improved atomization models.

2 Experimental details

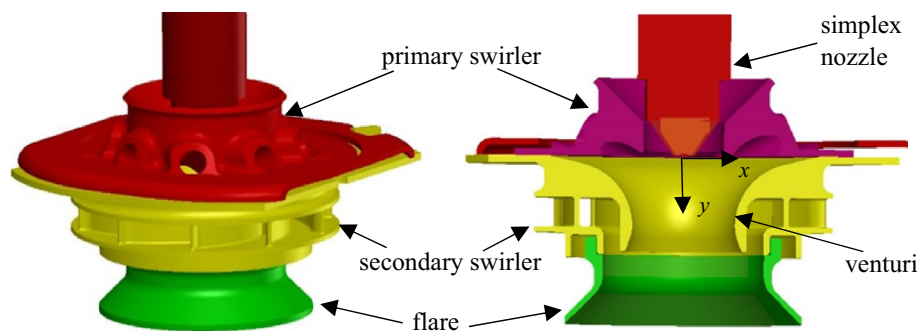
2.1 Geometries and flow conditions

A stage-wise measurement approach is adopted, to track the spray flow field as it passes through different regions of the swirl cup. For this, the swirl cup assembly is split into different configurations (Fig. 2), namely, Case 1: the simplex nozzle; Case 2: Case 1 + the primary swirler; Case 3: Case 2 + the venturi, Case 4: Case 3 + the secondary swirler; Case 5: Case 4 + the flare. The simplex nozzle used in all the above cases has a flow number of $1.2 \text{ lbm/hr}/\sqrt{\text{psi}}$.

Each of the different configurations is mounted on a spray test rig with the appropriate nozzle holders to supply the required air and liquid flows. Experiments are performed at atmospheric ambient conditions, with water as the test liquid. In Case 3 alone, the venturi is made out of plexiglass using a die of the same shape as the actual venturi in the swirl cup, to provide optical access. The thickness of the plexiglass venturi is maintained at 0.5 mm to minimize the optical distortions.

The liquid injection pressure is maintained at 4 ± 0.1 bar in all experiments. For each configuration and both before and after experiment, the mass flow rate is calculated by collecting the liquid for a known time to ensure that the above injection pressure delivers a water flow rate of 1.15 g/s within 2% error. An ALR of 16 is taken as the nominal flow condition (pressure drop $\sim 4\%$), about which it is varied in the range of 12–25 for the full swirl cup in the parametric studies. Accordingly, the air flow rate is controlled by the MFC (Alicat Scientific) with an error of $\pm 0.1\%$. The air flow velocities and Reynolds numbers for Cases 2–5 over the test ALR range are shown in Table 1. The Reynolds number is defined based on the exit velocity and exit diameter in each geometry, except in Case 5, we use the same definitions as in Case 4.

Fig. 1 Geometry of the swirl cup: assembly and cut section views



2.2 Optical diagnostics

The droplet size and velocity distributions of the spray are determined using a three-component PDI (Artium Technologies, USA). The PDI (Bachalo and Houser 1984) contains two transmitters that are positioned 30° and 35° off axis to the receiver. The first transmitter generates two pair of laser beams at different wavelengths and a third pair of beams is taken from the second transmitter. All the laser beams intersect at a common point called the “measurement volume” and the photodetectors in the receiver are focused at this point. The intersection of the laser beams forms interference fringes, and as the particles pass through it, the light is scattered as it crosses the bright fringe regions. Knowing the scattered light frequency and the fringe distance, the three components of velocity can be deduced from the signals from each pair of beams in the measurement volume. Further, the phase difference between the two Doppler burst signals from a particle follows a linear relationship with the particle diameter. Based on this, the droplet size is estimated from the detectors’ spacing and the phase shifts between the signals. The PDI system is mounted on a 3-axis traverse with a positioning accuracy of 0.05 mm.

Experiments are conducted at different axial locations for each configuration. Spanwise measurements are performed in steps of 2 mm to obtain the radial variation of the droplet size and velocity, along two perpendicular directions. In Case 2, the effect of the recirculation zone on the droplet size distribution is captured by traversing axially as well. A total of 50,000 samples is acquired in the annular spray regions, but it is limited to 5000 in the CTRZ, considering the lower number count there. The overall validation rates

are maintained above 95% for all the data. In Case 3, where bigger droplets are observed, the size of the measurement volume is adjusted up to $647.9 \mu\text{m}$. Droplets bigger than 1 mm are rejected because of their non-spherical nature. The uncertainty in the diameter measurements is $0.5 \mu\text{m}$ and the velocity measurements have an uncertainty of 1%.

The spray structure at the exit of each configuration is imaged in a time-resolved manner. A high repetition rate Nd-YLF laser (Litron, LDY series) with necessary sheet/volume optics is used to illuminate the spray field. Images are always acquired at 5 KHz using a high speed CMOS camera (Photron, FASTCAM SA4) with a 70–300 mm zoom lens (Sigma), unless mentioned otherwise. The spray structure and wall filming inside the venturi are captured by time-resolved laser induced fluorescence imaging (TR-LIF), so as to avoid internal reflections within the plexiglass venturi wall that would otherwise obstruct the view inside. Rhodamine 6G dye is used as the tracing medium, which is mixed with the water at a concentration of 200 mg/l, following Schubring et al. (2010). This dye has an absorption peak $\sim 530 \text{ nm}$ and an emission peak $\sim 566 \text{ nm}$, thus a narrow bandpass filter centred round the latter wavelength is used to collect the LIF signal.

A number of ways of laser illumination and imaging are adopted for the different configurations studied in the present work. These are:

1. In Cases 1, 2, and 5 (Fig. 3a shows Case 2), a laser sheet ($\sim 1.5 \text{ mm}$ thick) diametrically cuts across the exit of the nozzle–swirler assembly in the longitudinal plane, and the elastic scattering by the liquid is imaged.

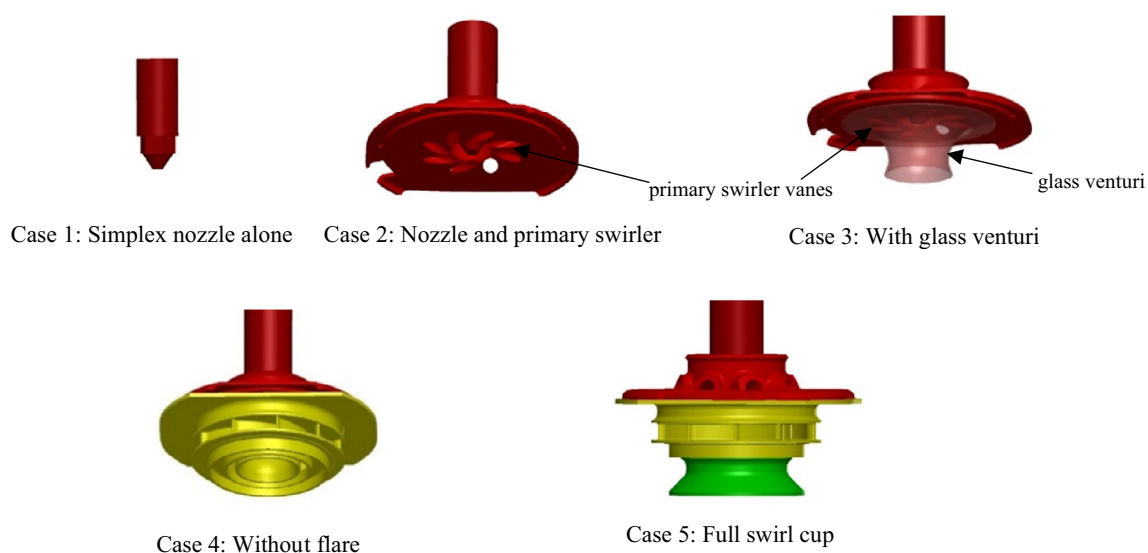


Fig. 2 Experimental configurations for the stage-wise characterization

Table 1 Air flow exit velocities and Reynolds numbers in the different cases

| No | Case | Exit velocity (m/s) | Reynolds number $\times 10^4$ |
|---------|-------------------|---------------------|-------------------------------|
| 2 | Primary swirler | 14–29 | 1.8–3.7 |
| 3 | Venturi | 19–40 | 2.2–4.5 |
| 4 and 5 | Secondary swirler | 20–42 | 3.5–7.3 |

2. In Case 3, four different illumination/viewing arrangements are adopted:
 - a. Time-resolved volumetric LIF (TR-VLIF) is adopted to examine the overall spray field features inside the venturi and the breakup of the liquid rim at the venturi tip (Fig. 3b); here, the round light beam from the laser head is converted into a cuboidal shape with a cross-section of 50 mm \times 50 mm, using a volume optics module (LaVision), to illuminate the entire venturi region.
 - b. TR-VLIF of the liquid rim at the tip of the venturi and the precession of the spray issuing out of the venturi, in an oblique view from the bottom (Fig. 3c).
 - c. A light sheet of 1 mm thickness in the longitudinal plane intercepts the transparent venturi diametrically, and TR-PLIF in the region of 4.74 \times 4.74 mm² window size close to the inner wall is imaged with a spatial resolution of 4 pixels/ μ m (Fig. 3e), using a long distance microscope (LDM), to measure the liquid film thickness on the venturi wall; the depth of focus with the long distance microscope is 96 μ m, which limits the line-of-sight integration effect.
 - d. The same light sheet as the above grazes tangentially along the throat of the venturi, and TR-PLIF of a region of the same window size and resolution is viewed orthogonal to the light sheet using the long distance microscope (Fig. 3d), to quantify the droplet impingement statistics on the prefilmer wall.
3. In Case 4, an oblique viewing arrangement using the zoom lens is adopted, but with two different illumination strategies:
 - e. Volumetric (cuboidal) light beam (Fig. 3f), to image the elastic scattering of the breakup of the liquid rim and ligament shedding off the venturi tip in the presence of the secondary swirling air.
 - f. Light sheet (\sim 1.5 mm thickness) diametrically illuminating the longitudinal plane (Fig. 3g) to measure the liquid rim thickness in the presence of the secondary air swirl.

Measurements in both temporal and spatial dimensions are made from the above time-resolved imaging. Quantities involving temporal measurement are the frequencies of droplet precession, ligament shedding, droplet impingement on the liquid film and film thickness oscillations. For these, the imaging rate of 5 kHz is sufficient in all cases. Quantities involving measurement in linear dimension are: the thickness of the liquid film on the venturi wall (Case 3, arrangement (2)c above, Fig. 3e), the size of the crater formed by droplet impingement on the liquid film (Case 3, arrangement (2)d, Fig. 3d), and the thickness of the liquid rim at the tip of the venturi (Case 4, arrangement (3)f, Fig. 3g).

For the purpose of calibration of the linear dimension in the images obtained with the long distance microscope (Case 3, arrangements (2)c and (2)d), a grid sheet of 100 μ m \times 100 μ m resolution is used. Since the venturi causes optical distortion along its three-dimensionally curved surface, five points on the grid sheet are chosen along the curved wall for calibration in arrangement (2)c, whereas the central region of the grid sheet is used for calibration in arrangement (2)d. In Case 4 with arrangement (3)f, the diameter of the venturi seen in the oblique view images is used for calibration of the linear dimension.

3 Results and discussion

3.1 Stage-wise spray characterization

The internal atomization characteristics of the swirl cup are investigated in a stage-wise manner using the different configurations mentioned earlier. PDI measurements are performed at the exit of each case and the time-averaged droplet size and velocity distribution for all the stages are given in Figs. 4 and 5.

3.1.1 Spray characteristics of the simplex nozzle

In Case 1, the simplex nozzle produces a 90° hollow cone spray, and majority of the droplets are present at the spray cone where the volume flux is maximum (Fig. 4a). The mean droplet size across the cone region is measured in the range of 31–36 μ m, and the SMD is in the range of 48.5–51.9 μ m. The velocity field of the simplex nozzle spray peaks at the spray cone, where the mean axial velocity is 8.79–11 m/s and the radial velocity is 8.6–9.9 m/s, whereas the tangential velocity is negligible.

3.1.2 Effect of the primary air swirl on the simplex spray

The structure of the spray in the presence of the primary swirling air (Case 2) is shown in Fig. 6. The primary air undergoes vortex breakdown and generates a central toroidal

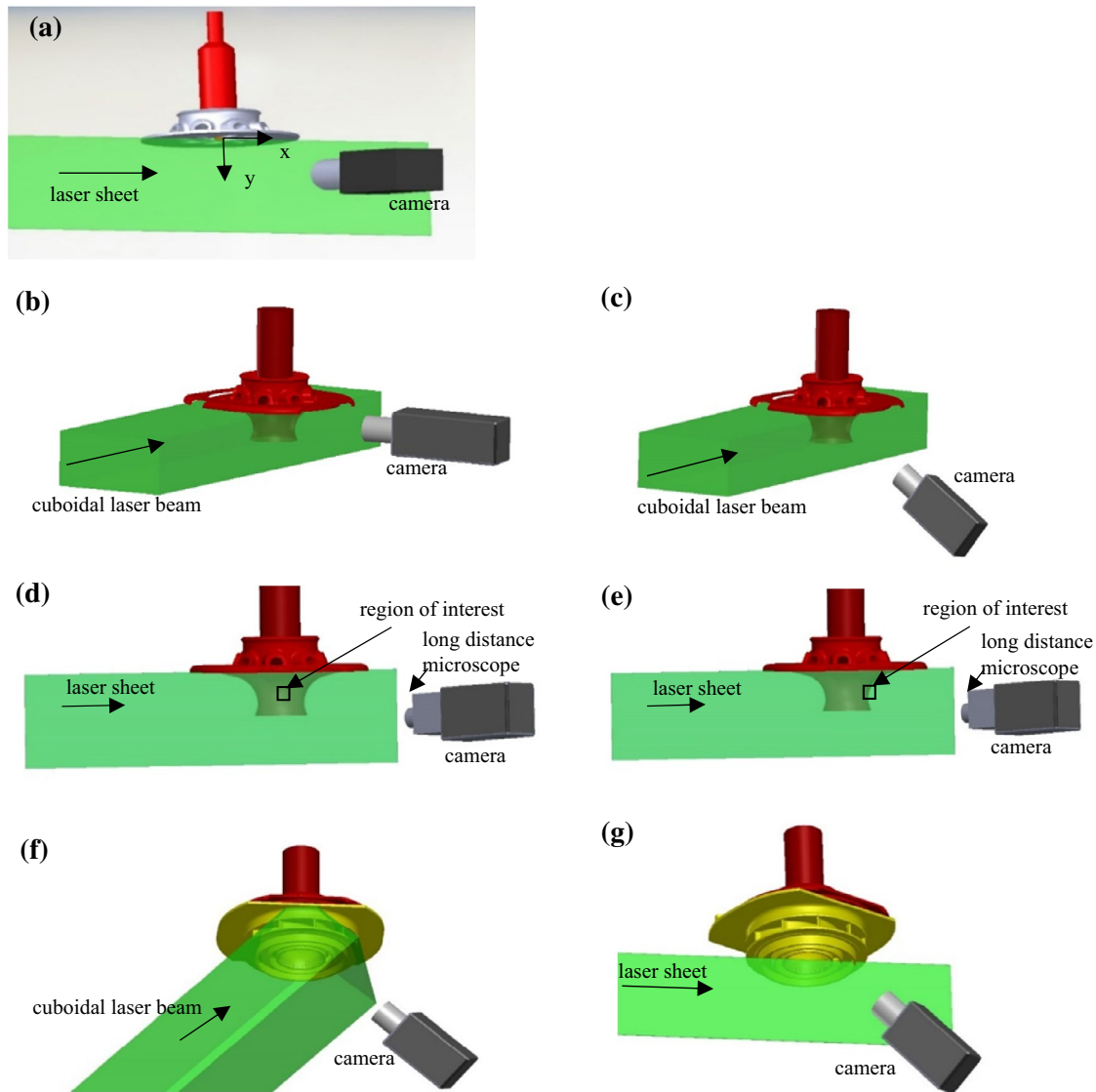


Fig. 3 Illumination and imaging views for different configurations

recirculation zone (CTRZ) that aids in stabilizing the flame. The primary air imparts considerable momentum to the simplex spray, and the mean axial, radial and tangential velocities reach a maximum at the spray shear layer. The air momentum dominates the droplet velocity field and dispersion. The recirculation zone originates just below the injector tip and extends far downstream. Further downstream of the recirculation zone, the droplets are dispersed more uniformly, and a clustered droplet motion is observed under the influence of the primary air. The variations of the droplet size and axial velocity along the axial direction for this case are shown in Fig. 7. The negative axial velocity of the droplets along the central axis indicates that the droplet recirculation starts 14 mm from the injector tip and extends up to 46 mm downstream.

At the shear layer (spray core), the SMD is measured as 26–32 μm . Comparing Fig. 4a, b, a significant reduction in droplet size is observed where the volume flux peaks. Further, the axial, azimuthal and radial velocities are maximum at the spray shear layer, as shown in Fig. 5. The instantaneous fluctuations in the local circulation at the shear layer can result in large changes in the local Weber number that leads to the droplet breakup (Rajamanickam and Basu 2017a, b). In the present case too, the axial and azimuthal shear lead to the breakup of the droplets in the shear layer region. In the central region and the outer periphery, there exists a strong size–velocity correlation, and droplet dispersion is a function of the individual droplet size.

The velocity distribution is represented based on different droplet size ranges in Fig. 8. Smaller droplets with $< 10 \mu\text{m}$ may roughly represent the gas phase velocity since they could faithfully follow the gas phase (Stokes number, $St \ll 1$). Figure 8a shows that droplet class up to $40 \mu\text{m}$ is entrained to the recirculation zone, however, their number count is less. Significant lag is observed in the swirl velocity component between the continuous phase and bigger particles in the shear layer region ($x/d = 0.4\text{--}0.5$), suggesting the momentum exchange in the azimuthal direction by the primary air. In the outer periphery ($x/d > 0.8$), the droplet size is found to increase gradually. The number count of these droplets is < 150 , with axial velocity and tangential velocities $< 5 \text{ m/s}$ there. The higher radial velocity and the lesser axial velocity

of the bigger droplets suggest that these droplets may have resulted from the coalescence of smaller droplets outside the spray core. This could explain the wetting of the venturi wall in the upstream region because of the spray impingement, as observed in Case 3 and discussed in Sect. 3.1.3.2.

3.1.3 Flow field inside the venturi

The internal flow field of the venturi is visualized using TR-VLIF imaging in the Case 3 configuration. An instantaneous VLIF image of the flow field is shown in Fig. 9a. The venturi acts as a confinement to this primary spray, and the region upstream of the throat is the zone where the primary spray is atomized. The droplets in the primary spray cone impinge

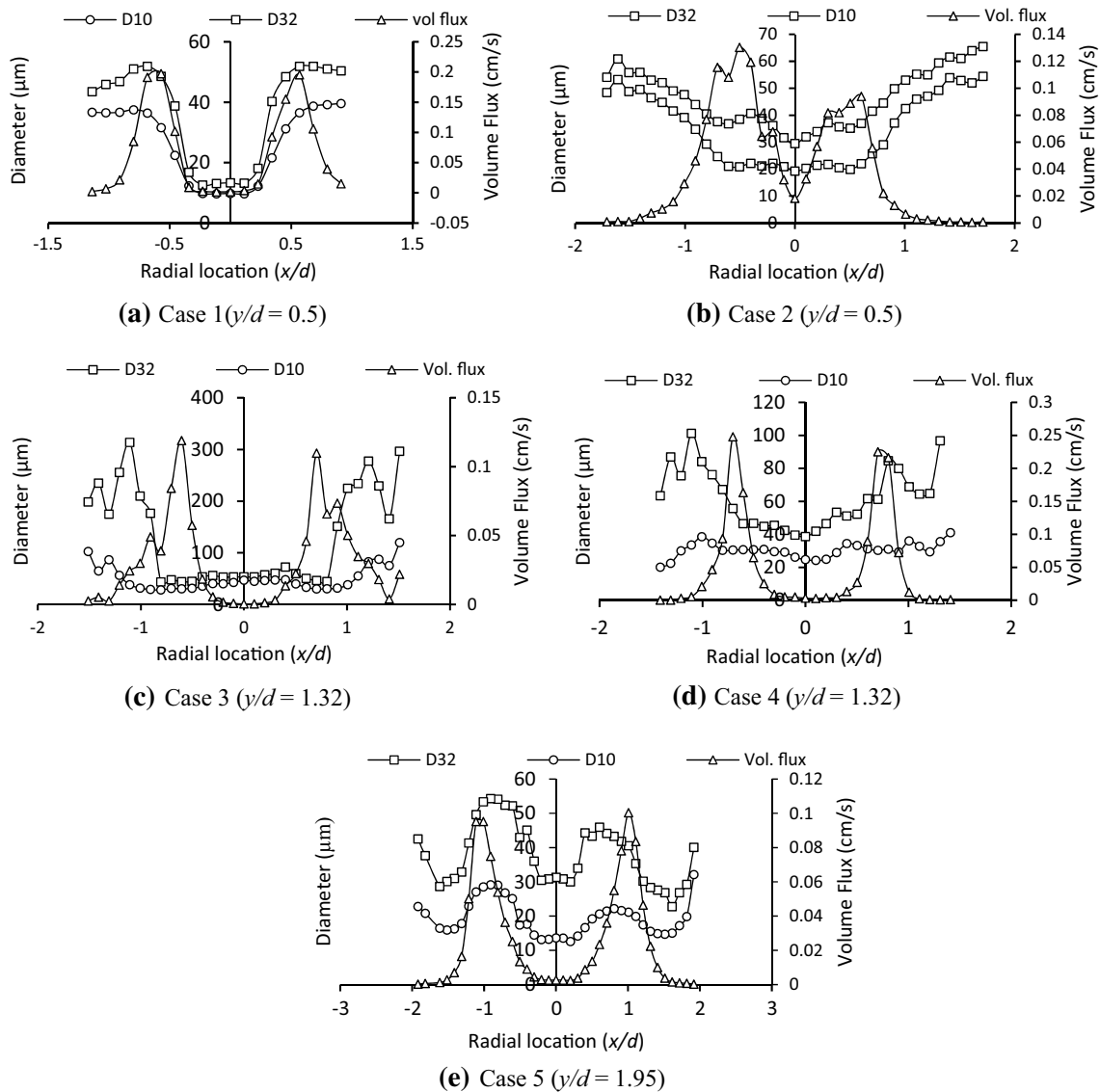


Fig. 4 Radial variation of droplet size at the exit plane in different cases

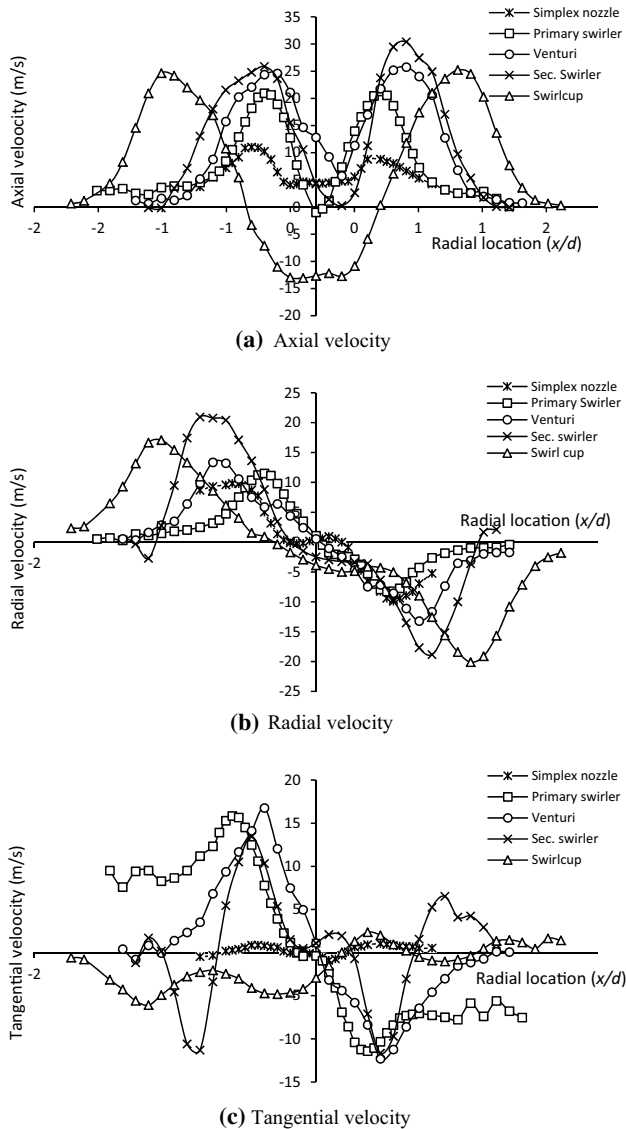


Fig. 5 Radial variation of velocity at the exit plane for all the cases

on the venturi surface, leading to the wall filming. The swirling primary air directs the droplets from the simplex nozzle spray to impinge nearly over the entire inner wall of the venturi. The resulting film appears as distinct streaks rather than a continuous film, as shown in the magnified view in Fig. 9b. The liquid film undergoes a spiral motion, driven by the primary swirl air, and accumulates into a thick liquid rim at the tip of the venturi. Since there is no secondary swirl air in Case 3, the above liquid rim extends over the outer wall of the venturi due to the Coanda effect.

The liquid rim disintegrates into strands extended at multiple azimuthal locations along the venturi tip. This process is shown in Fig. 10, as instantaneous snapshots. The liquid strands undergo flapping motion, and further break up into ligaments and droplets. These ligaments are further atomized

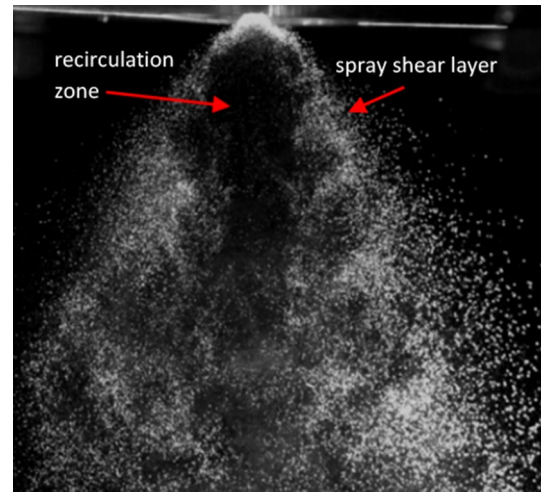


Fig. 6 Simplex nozzle spray in the presence of the primary swirl air flow (Case 2). The spray shear layer is the region where droplets align with the swirl shear layer, and the central hollow region is the recirculation zone to which smaller droplets are entrained

into smaller droplets by the aerodynamic interaction with the primary swirl air as they proceed downstream. A part of the liquid strands remains attached to the rim and further break up eventually into bigger droplets.

In addition to the droplets originating from the venturi tip, there exist fine droplets shedding periodically at the venturi exit, as marked in Fig. 9a. These droplets appear to emerge from the liquid film on the venturi wall upstream of the tip, and not from the accumulated rim. Investigations on planar atomizers (Inamura et al. 2012; Bhayaraju and Hassa 2009; Sattelmayer and Wittig 1986) have also revealed such droplet formation by the film shearing due to the formation of surface waves driven by the K–H instability, besides the large droplets shed from the prefilmer tip. In the present work, we find that, besides the above mechanism, the predominant process is the impingement of the primary spray droplets on the liquid film over the

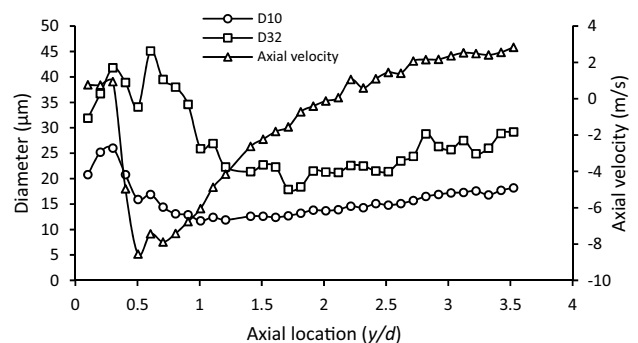


Fig. 7 Axial velocity and droplet size variation in the axial direction for Case 2

venturi wall, which causes splashing, and crater and crown formation. The secondary droplets at the tips of the crown are sheared off by the primary air swirl flow, leading to the shedding of the fine droplets alluded to above. The periodic nature of the shedding of fine droplets and the crater formation is related to the PVC of the air swirl, as will be detailed in Sect. 3.4. The details on the formation of craters during splashing and statistics of crater sizes are presented in the subsequent sections.

Figure 4c shows the radial variation of the droplet size at the venturi exit in the absence of secondary air. Even though the presence of the venturi acts as a confinement to the CTRZ, the hollow cone nature of the spray is preserved. Within the spray cone ($-0.8 < x/d < 0.8$), the SMD is measured in the range of 43.5–72 μm , and these droplets appear to have originated from the liquid film sheared by the primary air. Outside the shear layer ($x/d > 0.8$), the region where droplets are shed from the accumulated rim, the SMD is in the range of ~ 165 –314 μm with a number count < 50 . Further, there exists ligaments of considerably large in size > 1 mm, that are shed off the venturi tip somewhat quasi-periodically, which is not captured by PDI. This poor quality of atomization indicates that the primary air alone is insufficient to atomize the accumulated liquid rim at the venturi exit.

3.1.3.1 Droplet impingement and wall filming Even though the overall flow field is well captured by the TR-VLIF imaging, it is insufficient to resolve the wall filming process occurring at the venturi surface. Therefore, TR-PLIF imaging at high resolution using the long distance microscope is adopted to capture the wall filming (Fig. 3e) and droplet impingement (Fig. 3d) on it.

The unsteady wall filming process on a region of the venturi wall is illustrated in Fig. 11 as instantaneous images obtained at different instants. These images show that the film appears as distinct strips rather than a continuous film. The thickness of the film at a given location along the venturi wall also varies considerably at each instant. These features are due to the droplets from the primary spray impinging on the liquid film and either splashing to form craters or depositing on the film. The craters form crowns, which subsequently merge with the wall film after the secondary droplets at their tips, are sheared away by the air flow in the core of the venturi, as detailed earlier at the end of Sect. 3.1.3. The above events cause the film to appear as distinct strips with varying thickness in Fig. 11.

The crater formation due to droplet impingement is captured on the front region of the venturi wall, as shown in Fig. 12. The front face where the images are obtained is marked in Fig. 12a. The craters due to droplet impingement

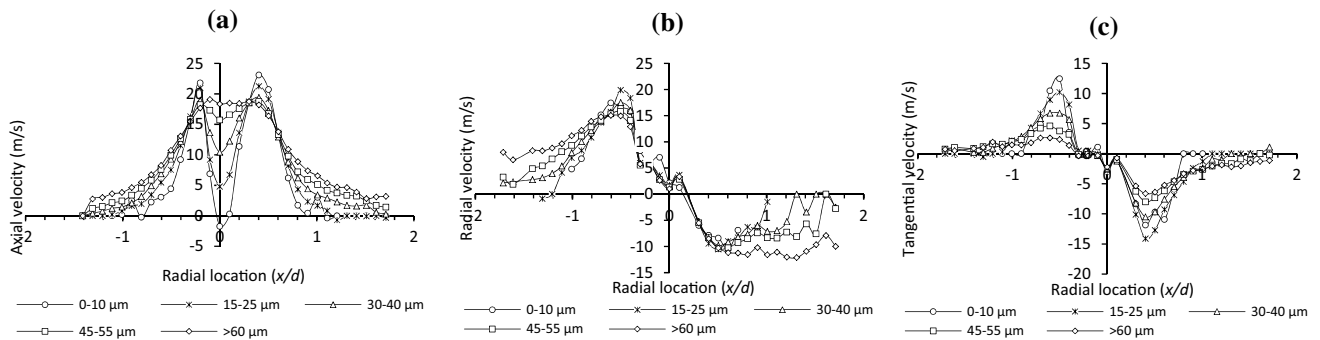


Fig. 8 Velocity distributions in Case 2 configuration for different droplet classes

Fig. 9 a Instantaneous VLIF image showing wall filming inside the venturi. b Magnified view of the venturi wall region showing the liquid film as distinct streaks

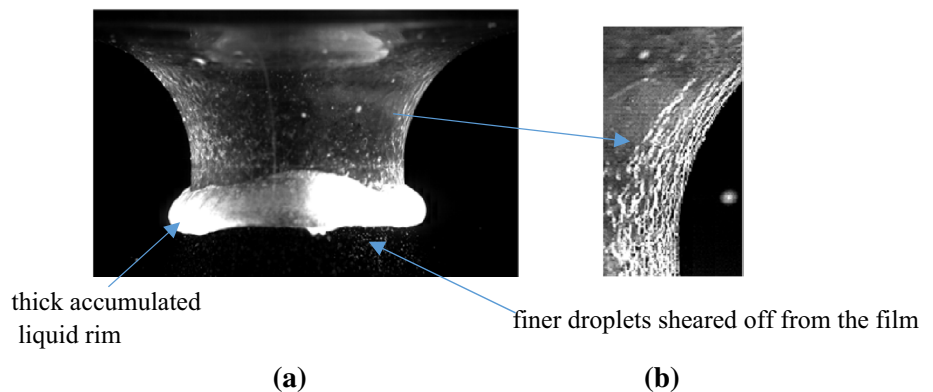


Fig. 10 Instantaneous snapshots of ligament shedding process at the venturi tip

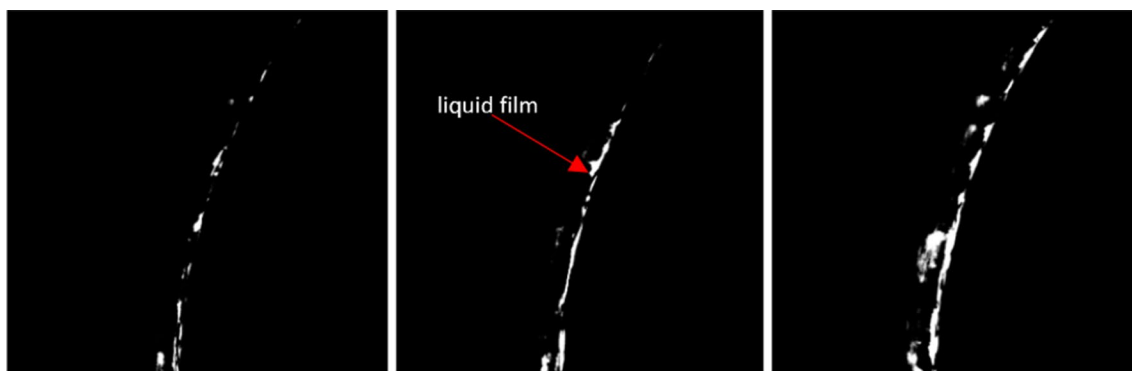
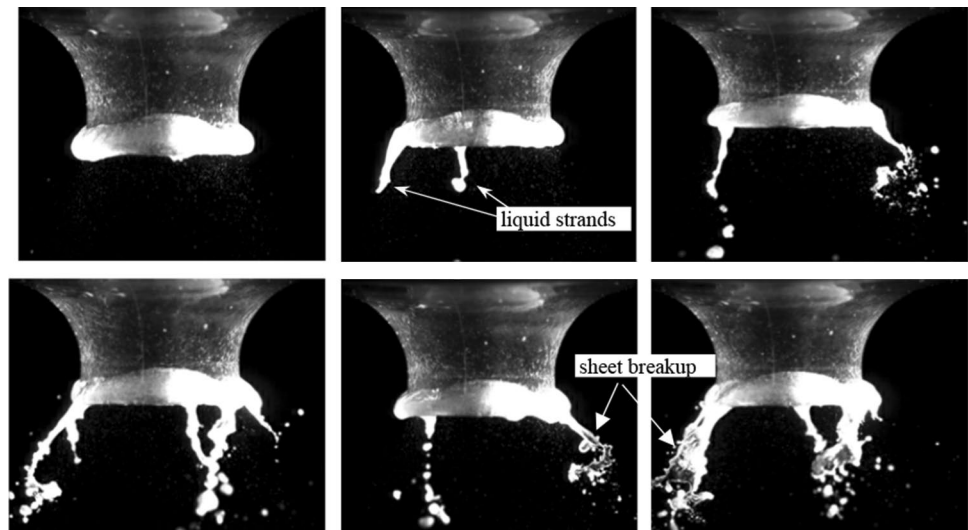


Fig. 11 LDM–PLIF image showing the unsteady wall filming process on a region of the venturi wall

formed are shown in the magnified view in Fig. 12b. The droplet number density of impingement is higher just above the venturi throat and decreases further downstream. The droplet impingement also results in the formation of air bubbles within the liquid film due to the entrainment of air. Schubring et al. (2010) have reported such bubble entrainment in coaxial thin film flows.

The co-flowing primary air causes surface K–H waves on the wall film, which grow both in the axial and azimuthal directions due to the swirling air flow. These waves undergo sufficient spatial amplification so as to be observable near the venturi tip, but their view is hindered by the local oscillations from the droplet impingement that dominates the film dynamics.

3.1.3.2 Estimation of the film and rim thicknesses The average film thickness over the venturi wall is estimated from the LDM–PLIF images in the Case 3 configuration. Since the long distance microscope covers only a region of $4.74 \times 4.74 \text{ mm}^2$, the entire venturi is divided into five regions 1–5, as

shown in Fig. 13a. The average film thickness variation as seen in these five regions along the venturi wall is shown in Fig. 13b–f. These are obtained by averaging over 5000 images each. Since the fluorescence from the liquid alone is captured in these images, the film thickness is estimated as the distance between two points with sharp gradients in the fluorescent intensity. This is demonstrated in Fig. 13e by a line along which the fluorescent intensity is mapped for examining the sharp gradients. The intensity profile thus obtained is shown in Fig. 14, where the sharp gradients are identified for estimating the film thickness. The uncertainty in the film thickness measurement is estimated as $8 \mu\text{m}$.

The spatial variation of the average film thickness is estimated in steps of 0.3 mm all along the venturi wall. Considering the venturi throat diameter d as the linear reference dimension, the variation of the average film thickness along the venturi wall is plotted against the normalized location z/d in Fig. 15, where z is the local axial variable starting from the top of the venturi, as indicated in Fig. 13. The standard deviation in the film thickness is plotted as the

error bar. The film thickness is measured within a region of $0.14 \leq z/d \leq 0.68$ along the venturi wall, with the venturi throat being located at $z/d=0.6$, for reference. Measurements could not be made beyond $z/d=0.7$ because of the thick liquid rim formed at the venturi tip obstructing the view, in the Case 3 configuration here.

As seen in Fig. 15, the wetting just starts in the upstream region (at $z/d=0.14$), and film thickness there is found to be minimal, at $27.5 \mu\text{m}$ for the nominal case of $\text{ALR}=16$. Subsequently downstream, the film thickness increases along the venturi wall because of the liquid added by the droplet impingement. The film thickness attains a maximum of $165 \mu\text{m}$ at a distance of $z/d=0.53$ from the tip for the above ALR, for instance. This location is still upstream of the venturi throat, but the film thickness begins to decrease further downstream as one approaches the throat and beyond. In the vicinity of the throat, the axial velocity component is high, which results in maximum shear (Wang et al. 2007), leading to the reduction in the film thickness, down to $122 \mu\text{m}$ for $\text{ALR}=16$ at the throat. Further downstream, the film starts to accumulate at the tip and forms a thick liquid rim.

3.1.3.3 Crater size distribution The crater size on the venturi wall represents the amount of liquid added to the pre-filmer and number of the secondary droplets generated. It is mainly influenced by the size of the impinging droplets. Here, we attempt to estimate the crater size distribution from the LDM–PLIF images of the front wall of the venturi, one of which is shown in Fig. 12b. Accurate measurement of the crater size is challenging since the craters are often non-circular, and some of them are at different stages of splashing at any instant of imaging, resulting in many different impressions they imprint on the liquid film. Besides this, craters are to be identified as distinct from the bubbles

around them in the image processing. This is accomplished because of the distinct difference in their intensities in the images, however.

A series of image processing steps are adopted to extract mainly round craters, eliminating partial ones, bubbles, other blobs, and similar other features on the film surface. A circularity of 0.7 is kept as the threshold value and craters of area $> 5100 \mu\text{m}^2$ are selected for the analysis based on the possibility to accommodate most of the relevant craters. The histogram showing the crater size distribution is given in Fig. 16a for $\text{ALR}=16$. For comparison, the droplet size distribution measured at the shear layer locations along the primary swirler exit (Case 2) is shown in Fig. 16b. It is observed that droplets in the range of $10\text{--}50 \mu\text{m}$ from the primary spray create craters in the size range of $100\text{--}250 \mu\text{m}$, with an arithmetic mean of $186 \mu\text{m}$.

Spray impact on a wet wall is quite a complicated phenomenon and involves several sub-processes such as multiple drop impact, splashing, crater formation, secondary drop formation, local film oscillations, and film transport in presence of cross-stream air flow. These flow processes are coupled to each other and the interrelated processes are very difficult to understand and model. Several investigations are reported in the literature on drop/spray impingement on a wet/dry wall, but a comprehensive understanding is yet to be developed considering the unknown flow parameters. The present scenario is a spray impact to a thin liquid film in the presence of a swirling air streams. Roisman et al. (2008) modelled the single drop impact on a thin film and the crater formation process using a kinematic discontinuity approach. We have attempted to implement this particular model to predict the crater size and to compare with the experimental data. The primary spray characteristics obtained with the configuration of Case 2 is used as the input spray parameters, even though

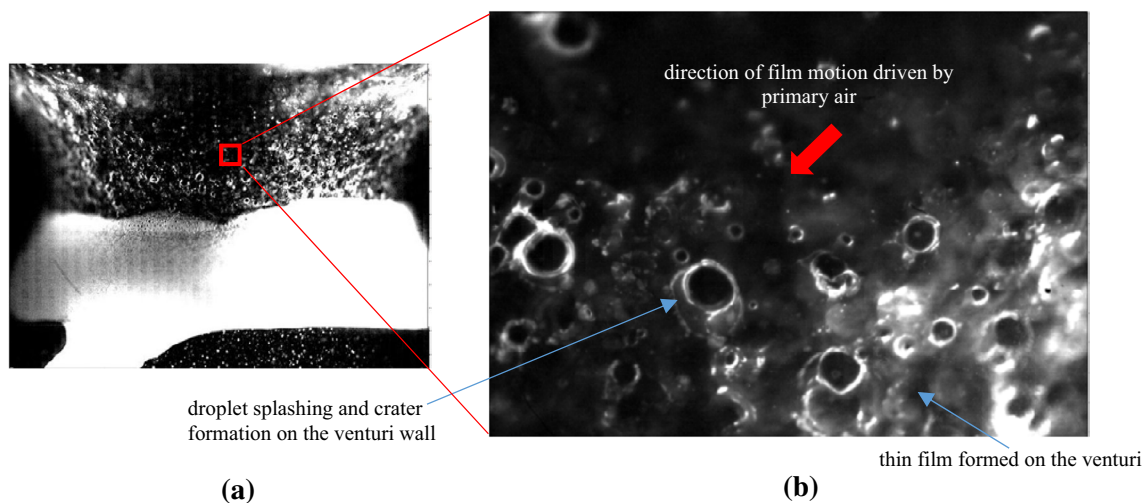


Fig. 12 **a** Instantaneous VLIF image showing droplet impingement. **b** LDM–PLIF image showing the droplet splashing in a magnified view

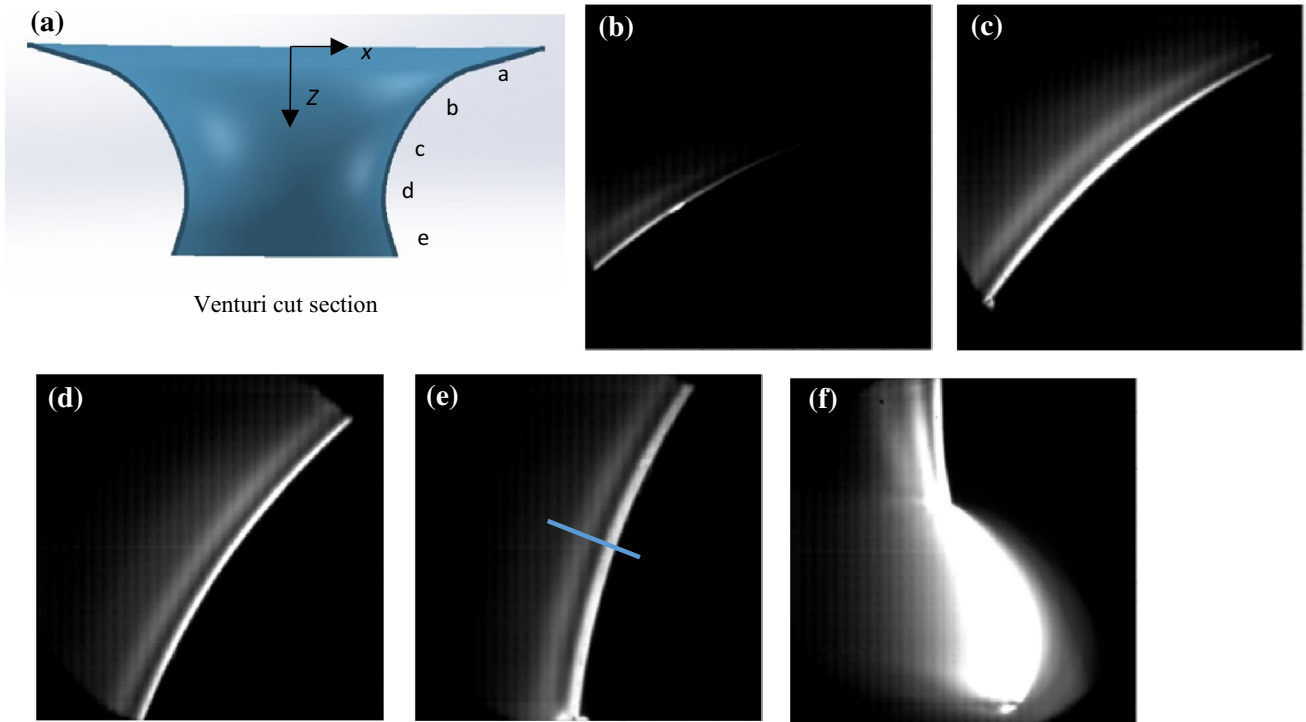


Fig. 13 Film thickness variation over the venturi surface covering five regions

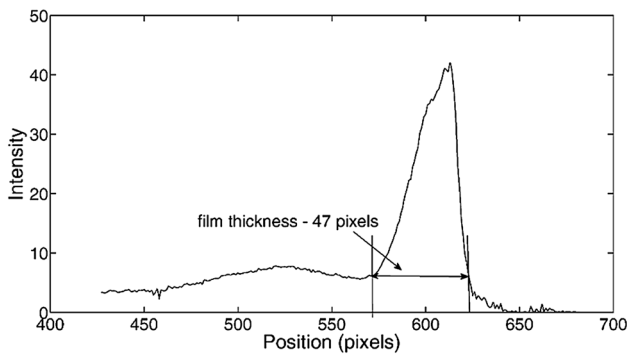


Fig. 14 Fluorescent intensity profile across the liquid film thickness in Fig. 13e

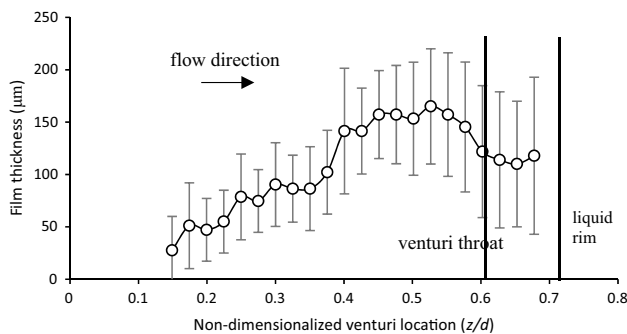


Fig. 15 Film thickness variation over the venturi surface at ALR = 16

the venturi confinement alters the primary spray. Representative droplet size, velocity and non-dimensional numbers are given in Table 2. The film and impingement data given here are measured $y/d=0.43$ location of the venturi wall. The non-dimensional numbers are estimated as follows:

$$\text{Non-dimensional film thickness, } H = \frac{H^*}{D_p^*}, \tag{1}$$

$$\text{Crater Weber number, } We_{cr} = \rho_g U^{*2} D_p^* / \sigma, \tag{2}$$

$$\text{Ohnesorge number, } Oh = \frac{\mu}{\sqrt{\sigma \rho D_p^*}}, \tag{3}$$

$$\text{Froude number } Fr = \frac{U^{*2}}{(g D_p^*)}, \tag{4}$$

$$\text{Reynolds number } Re_l = \frac{\rho_l U^* D_p^*}{\mu_l}, \tag{5}$$

where U^* is the impact velocity, D_p^* is the impact droplet size, H^* is the film thickness at $y/d=0.43$, σ is the surface tension, μ_l is the viscosity of the liquid, ρ_g and ρ_l are the density of the air and liquid. Further, normal impact is assumed at $y/d=0.43$, since the venturi is a curved surface, although the

impact angle is not known. The measured crater size represents the maximum possible crater size, since partial or uneven craters are eliminated during image processing. Gravity effects are neglected in comparison with the surface tension forces and considering the smaller droplet size < 100 μm.

As per the model (Roisman et al. 2008), the maximum crater size $R_{cr,max}$ at the maximum receding time τ_{max} is estimated as

$$R_{cr,max} = \frac{\beta \sqrt{H We_{cr}} - H}{4}, \tag{6}$$

where β is the parameter which is a function of the non-dimensional film thickness. The crater size $R_{cr,max}$ measured and the predicted crater size are plotted in Fig. 17. It can be seen that the present data compares remarkably well with the prediction from the above model. This implies that despite the simplified conditions of single droplet impingement considered for the model development, the major influencing factors in the process are captured by the model, sufficient to correlate well with the present conditions of a complicated flow field.

The prediction of the film thickness based on the flow parameters is very important but less explored, considering the number of unknown parameters and coupling of the

related processes. The film motion involves the shearing action of the swirling air in the axial–tangential direction and the oscillations induced by the impinging droplets. We have attempted to apply the models by Roisman et al. (2008) and Batarseh (2008) to the present data based on the initial parameters such as Weber number and Reynolds number. The model considers single drop impact on a thin film and the maximum receding time of the crater can be expressed as

$$\tau_{max} = \frac{\beta H We (\beta \sqrt{We} - H)}{8 (\beta \sqrt{We} + H)}. \tag{7}$$

The film thickness is assumed to scale with the thickness of the oscillating viscous boundary layer on the film surface, which can be represented as,

$$H_{\theta} \sim \sqrt{(\vartheta \tau_{max})}. \tag{8}$$

Solving the above equation results in

$$\frac{H_{film}}{D^*} \sim \left(\frac{We}{Re} \right)^{3/4}. \tag{9}$$

Fig. 16 Comparison of crater size and primary spray droplet size distribution

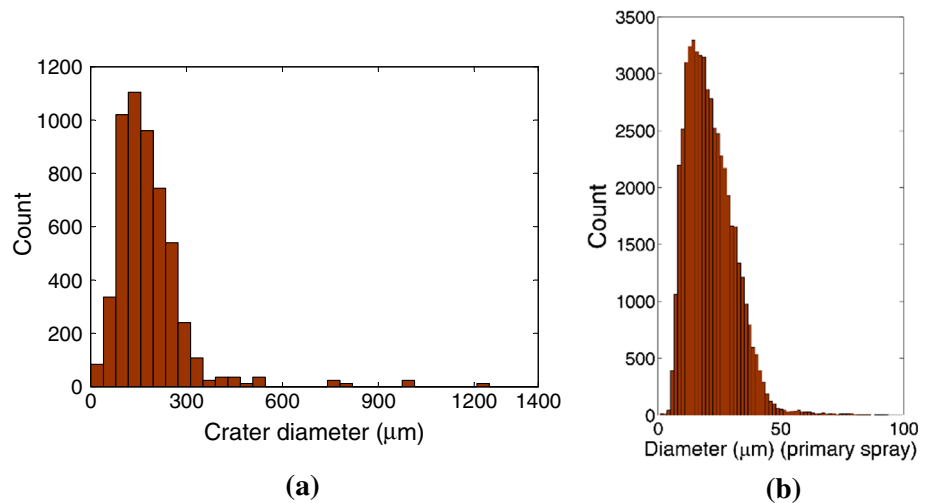


Table 2 Spray impingement parameters and non-dimensional numbers

| Air velocity (m/s) | D_p^* (μm) | U^* (m/s) | H^* (μm) | H | We_{cr} | Re_l | Fr | β |
|--------------------|--------------|-------------|------------|-----|-----------|----------|-----------|---------|
| 19.3 | 36.5 | 13.88 | 153.27 | 4.2 | 98 | 27440.61 | 531109.1 | 1.44 |
| 22.5 | 32.4 | 16.19 | 148.96 | 4.6 | 118 | 28314.19 | 817360.6 | 1.29 |
| 25.8 | 26.3 | 18.50 | 141.48 | 5.4 | 125 | 26327.5 | 1,312,152 | 1.37 |
| 29.0 | 23.6 | 20.81 | 133.62 | 5.7 | 142 | 26550.28 | 1,852,603 | 1.19 |
| 32.2 | 19.1 | 23.13 | 121.26 | 6.3 | 142 | 23950.28 | 2,817,171 | 1.29 |
| 40.3 | 14.5 | 28.91 | 83.46 | 5.7 | 169 | 22720.91 | 5,800,001 | 1.29 |

The term $\frac{We}{Re}$ is called the capillary number Ca , and hence, the non-dimensional film thickness can be as expressed as a function of Ca ,

$$H = Ca^{3/4}. \tag{10}$$

Measured dimensionless film thickness H is represented as a function of Ca in Fig. 18 for the test range considered here. Up to $ALR = 20$, the data scales linearly, and for the $ALR = 25$ case, a deviation in the trend is noted. This could be because as the ALR increases, the film shearing increases, which affects the impingement/ film formation process. Further data may have to be obtained to ascertain this mechanism in a systematic manner.

3.1.4 Atomization at the secondary exit

The ligament breakup process at the venturi tip in the presence of the secondary air is investigated in Case 4. Since the perpendicular view to the venturi region is obstructed by the secondary swirler, the venturi tip is focused at an oblique angle viewed from the downstream (refer Fig. 3f). Figure 19a shows that in presence of the secondary air, the film accumulation into the liquid rim at the venturi tip is circumferentially more uniform. The shear layer formed at the venturi exit by the counter-rotating air streams reduces the accumulation time of the liquid rim, resulting in the formation of a relatively thinner rim when compared to the case without the secondary air swirl (Case 3) considered before (Fig. 9a). This thinner liquid rim breaks up into many small liquid strands, and their shedding occurs quite uniformly all around the tip. From this, it is clear that the counter-rotating swirl shear layer at the venturi exit plays a major role in dictating the liquid rim size and its subsequent atomization. Further, the average image in Fig. 19b shows a uniform film and liquid rim, suggesting that the liquid film and the

process of liquid rim breakup do not carry the memory of the swirl vane wakes.

In this case, the breakup of the liquid rim at the venturi tip is hugely aided by the counter-rotating swirl flow of air on either side. Surely, the accumulated liquid rim rotates in the clockwise direction following the sense of the primary air swirl, but it gets extended into liquid strands at multiple points in the anti-clockwise direction by the secondary air. These strands are evidently much thinner and more sporadic than those observed without the secondary air in Case 3 (Fig. 10). Parts of the liquid strands are sheared due to the counter-swirl air flow into liquid sheets as pointed out in Fig. 19a, followed by a wavy sheet breakup of such sheets. The remaining part attached to the rim directly breaks up into a cluster of ligaments of varying sizes at multiple locations, as also marked in Fig. 19a. This primary atomization process is completed and finer droplets are formed within a few millimetres from the venturi tip. During this process, the fine droplets continue to emerge from the liquid film at the venturi wall and passing through the core of the venturi exit as before (Fig. 9a), undisturbed by the secondary air swirl flow.

It is also evident from the LIF images that the major source of droplet origin in the swirl cup is the accumulated liquid rim and not the wall film. The size of the rim and the shear layer decide the size of the majority of the droplets at the swirl cup exit. Further, it can also be concluded that the droplet origin at the venturi exit is of two classes. One from the venturi tip, controlled by the shear layer of the counter-rotating air streams, and the other from the film shearing, which is dictated by the primary air PVC (discussed in detail in Sect. 3.4).

The rim formation and ligament breakup are visualized for different ALR in the range of 12–25, and instantaneous image in each case is shown in Fig. 20. As the ALR increases, the rim thickness decreases, and the ligament shedding from the rim becomes more uniform, thus

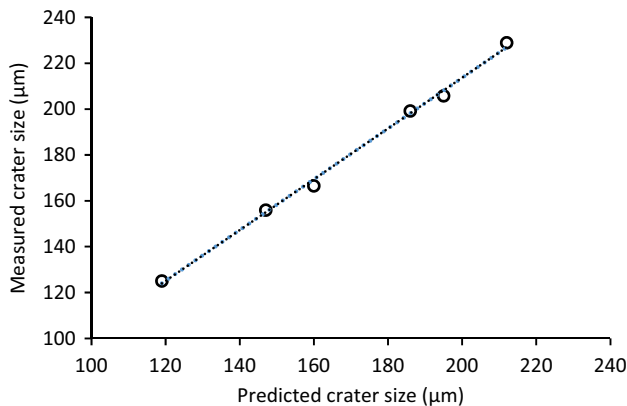


Fig. 17 Comparison of the theoretical crater diameter to the measured data

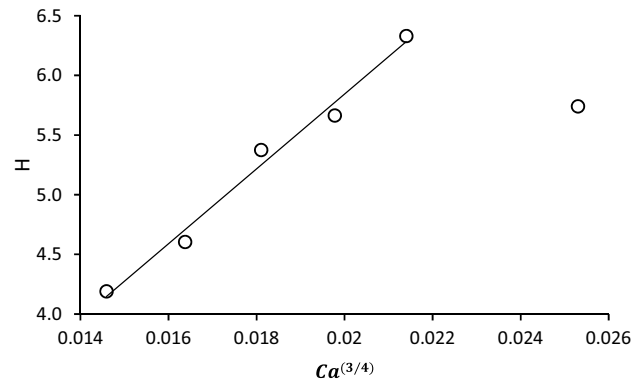


Fig. 18 Dimensionless film thickness as a function of capillary number

generating smaller droplets. Further, at large ALR, the fine droplets from the primary spray, as well as those emerging from splashing against the wall film, are entrained into the swirl air flow inside the venturi, causing a spiral wave of clustered droplets due to the PVC of the swirl flow. This is highlighted specifically for $ALR = 25$ in Fig. 20c.

As mentioned earlier, the accumulated liquid rim is the major source of further droplets downstream, and the thickness of the liquid rim is representative of the amount of liquid accumulated in it. Hence, the liquid rim thickness is measured from the PLIF images (Fig. 19b), in the configuration of Case 4, as this is with the secondary swirl air flow and provides a more realistic estimate relative to that seen in Case 3 (Fig. 9a). The liquid rim thickness is defined as the average thickness measured of the high PLIF intensity region of the accumulated rim at the tip viewed at an oblique angle, as shown in Fig. 21. The estimated thickness is corrected for the image distortion in the oblique view. The uncertainty in the rim thickness measurement is $48 \mu\text{m}$. The liquid rim thickness at the venturi tip is estimated as $1660 \mu\text{m}$ for the nominal case of $ALR = 16$, which is considerably higher than the corresponding film thickness.

The size distribution of the droplets originated from the liquid rim is shown in Fig. 4d and the corresponding three-component velocity distribution of different droplet classes at the venturi exit is plotted in Fig. 22. In case of axial and radial velocities, the average values increase progressively from the centre line since both primary and secondary air imparts axial and radial momentum in the same direction (Fig. 5a, b). The width of the shear layer is in the range $0.4 < x/d < 1.1$ based on the gas phase velocity gradient. With the secondary air swirl present, two tangential velocity peaks are observed within the shear layer as seen in Fig. 5c. At $x/d = 0.5$ from the centreline near the inner edge of the shear layer, there exists a mean tangential velocity peak of $11\text{--}13 \text{ m/s}$, where droplets circulate in the clockwise

direction looking along the axial direction (the direction of the primary air swirl). At the outer edge of the shear layer ($x/d = 0.9\text{--}1.1$), a second velocity maximum exists with a tangential velocity in the range of $6\text{--}11 \text{ m/s}$, where the droplets circulate in the anti-clockwise direction (the direction of the secondary air swirl). Most of the droplets are atomized within the shear layer as seen in the distinct volume flux peaks in Fig. 4d. The atomization of the liquid rim in the presence of the shear layer results in a substantial improvement in atomization compared to case 3 and the SMD is measured in the range of $46\text{--}67 \mu\text{m}$ in the shear layer region, 10 mm from the venturi exit. The inner shear layer region is populated by relatively smaller droplets ($< 30 \mu\text{m}$) from the primary spray, but bigger droplets from the venturi tip ($> 30 \mu\text{m}$) populate the outer region.

Further, within the shear layer itself, there is a significant momentum exchange to the liquid phase from the shear layer. The axial and radial velocity field of smaller droplets $< 40 \mu\text{m}$ is dominated by the gas phase momentum as observed in Fig. 22a, b. Within the inner shear layer region, smaller droplets $< 40 \mu\text{m}$ rotate in the same direction of the primary air swirl, since they follow the gas phase, and in the outer shear layer region ($x/d \sim 1.1$) bigger droplets $> 45 \mu\text{m}$ rotate in the secondary air swirl direction (Fig. 22c). The bigger droplets from the rim penetrate through the shear layer and follow the secondary air swirl direction, and the majority of the smaller droplets carrying lesser momentum gets trapped within the inner primary air flow.

3.1.5 Spray characteristics at the swirl cup exit

At the swirl cup exit, droplets are well atomized and the SMD is further reduced to $44\text{--}53 \mu\text{m}$, as seen in Fig. 4e. This is by means of the aerodynamic interactions with both the swirling air streams. The droplet size range at the swirl

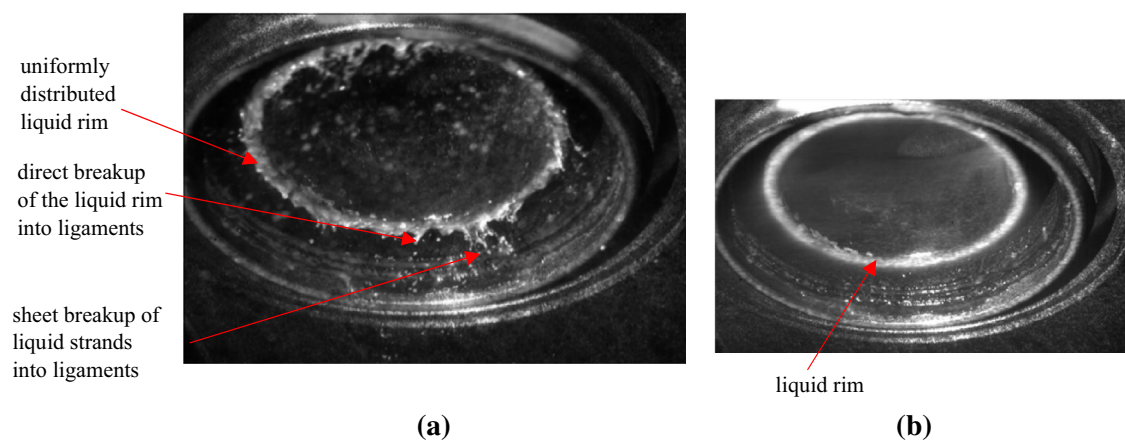


Fig. 19 **a** Instantaneous and **b** averaged VLIF images of ligament breakup at the venturi tip (Case 4)

cup exit matches quite well with that reported by Jeng et al. (2004) for similar flow conditions.

At the swirl cup exit, the recirculation zone further expands as the flow issues out of the flare. There is a small reduction in the axial velocity. The interaction of the counter-rotating air swirl streams results in a reduction of the tangential velocity component with a velocity peak of ~ 5 m/s at the swirl cup exit (Case 5) as compared to the velocity values of 12–14 m/s observed in Case 4. The secondary flow dominates the swirl sense, thus a majority of the droplets at the exit of the swirl cup circulate in the anti-clockwise direction looking along the streamwise (axial) direction.

However, within a region inside the recirculation zone, the droplets still circulate in the clockwise direction, preserving their sense of the primary air swirl. Figure 23 shows the velocity field corresponding to the individual droplet classes. At the spray shear layer ($0.7 < x/d < 1.4$), the bigger droplets ($> 45 \mu\text{m}$) have maximum axial and radial velocities as they carry more momentum. The tangential velocity field (Fig. 23c) shows all range of droplet class inside the spray shear layer, suggesting that swirl cup spray provides efficient mixing as the spray issues out of the flare.

In general, the overall spray structure (droplet dispersion, entrainment, and width of the spray) is influenced by the

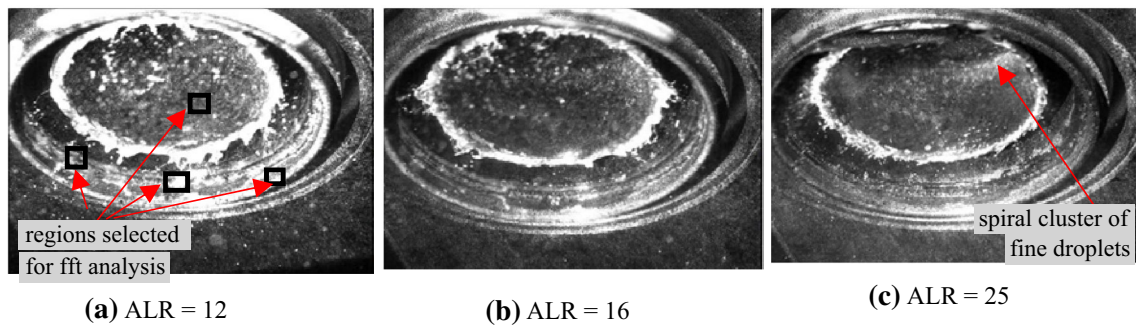


Fig. 20 Atomization at the venturi tip at different ALR

Fig. 21 Average PLIF image showing the rim thickness

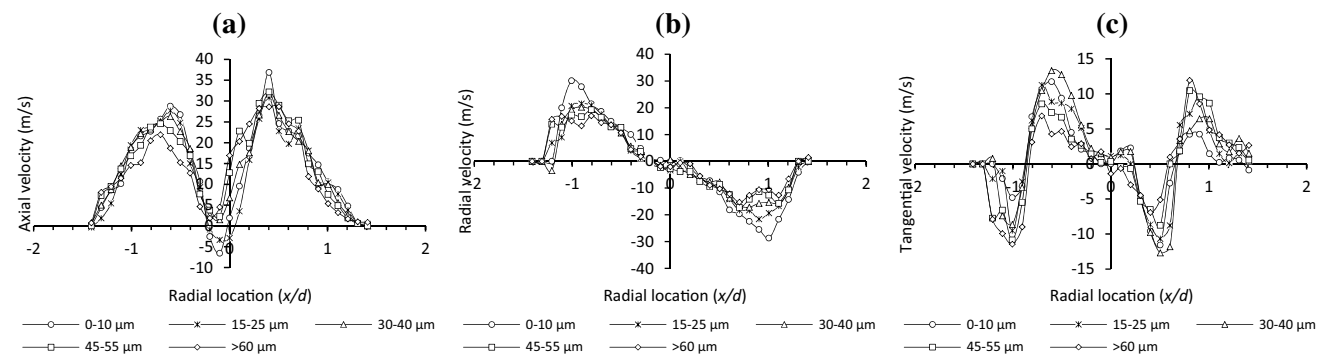
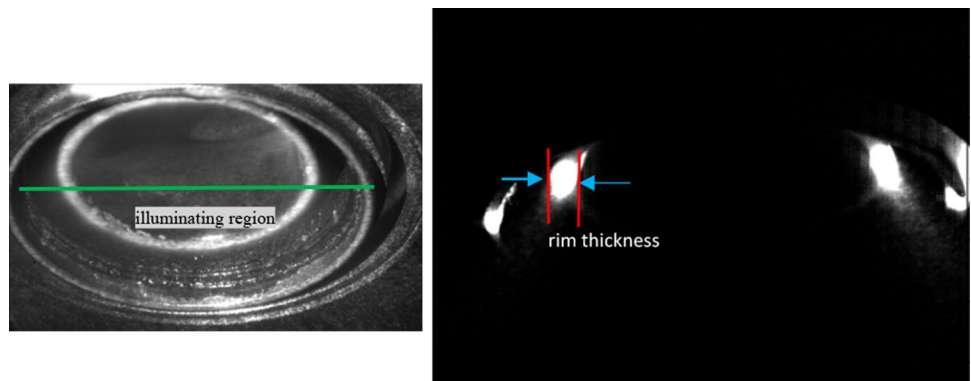


Fig. 22 Velocity distributions in Case 4 configuration for different droplet classes

CTRZ of the primary swirl air flow. The shear layer between the primary and secondary counter-rotating swirl air flows mainly helps to improve the atomization and mixing. The spray velocity field at the swirl cup exit is decided by the combined action of the CTRZ and the shear layer.

3.2 Consolidation of the measured quantities

In this work, we have quantified various atomization processes inside the swirl cup and acquired statistics at different points inside. This helps to understand how the internal two-phase flow progresses at different stages of the swirl cup. The primary spray generates droplets in the size range of 15–35 μm for the range of ALR considered here. The variation with respect to ALR of the further measurements subsequently downstream, namely, the film thickness and crater size at a spray impingement location of $y/d=0.45$, is shown in Fig. 24.

It can be seen from Fig. 24 that the droplet impingement at this location results in the formation of craters with a size range of 119–212 μm as the ALR decreases from 25 to 12. As the air flow rate increases, the primary spray droplet size decreases, because of the higher aerodynamic forces. This results in the formation of smaller craters, even though the impingement velocity is higher with an increase in the air flow rate. At higher air flow rate, the droplet impingement density also reduces, which is evident from the LIF images. The resulting liquid film has a thickness that varies from 153 to 83 μm. The reason for the reduction in the film thickness is mainly twofold. First, at higher air velocities, the primary spray droplet size becomes smaller, and a part of them is carried away along with the primary air as a helical cluster of droplets influenced by the PVC (Fig. 20c). Subsequently, the amount of liquid added to the venturi wall reduces, resulting in a thinner liquid film. Second, air flow at higher velocities shears off the film further, resulting in a decrease in the

film thickness. This effect is more predominant as the film approaches the venturi neck.

The variation of the liquid rim thickness is also shown in Fig. 24. The rim thickness varies from 915 to 2200 μm as the ALR is decreased. It is also to be noted that the rim thickness is higher than the film thickness by an order of magnitude. Further, the rim thickness is a function of air velocities, liquid flow rate, accumulation time, and the shape and thickness of the prefilmer tip.

At the swirl cup exit, the SMD is in the range of 25–55 μm. This shows that the swirl cup spray gets well atomized by the shear layer generated by the counter-rotating air swirl and the subsequent aerodynamic interaction as the flow passes through the flare.

3.2.1 Global SMD

The progress in the atomization as the flow passes through the swirl cup can be assessed by the volume flux averaged SMD, referred to as the global SMD (GSMD) (Bhayaraju and Hassa 2009). The GSMD can be defined as the local volume flux averaged SMD taken along the radial direction (x -axis, as shown in Fig. 3a) as

$$GSMD(y) = \frac{\sum_{x=i}^{x=n} V_i(x, y) SMD_i(x, y)}{\sum_{x=i}^{x=n} V_i(x, y)} \tag{11}$$

Here, V_i indicates the local volume flux at each radial measurement location x_i for any given axial distance y from the exit plane of the geometry in each case.

Further, the gas Weber number also represents the atomization at every stage. It is defined as

$$We_g = \frac{\rho_a V_R^2 D_0}{\sigma} \tag{12}$$

where ρ_a is the air density, D_0 is the initial diameter, V_R is the relative velocity between air and liquid and σ is the surface tension of the liquid.

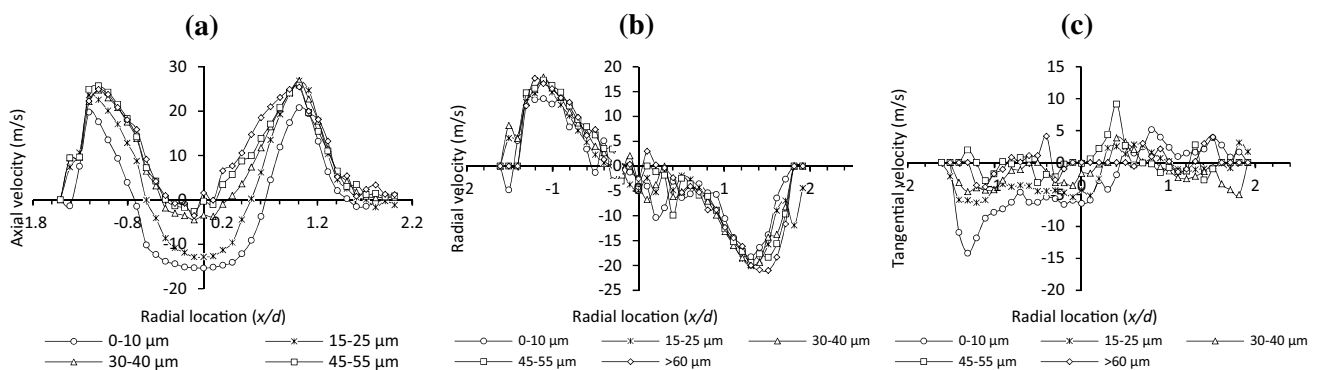


Fig. 23 Velocity distributions in Case 5 configuration for different droplet classes

Table 3 shows the comparison of the droplet size in terms of the GSMD and $SMD_{peak\ data\ rate}$, so that its variation for the different configurations can be considered in the discussion below. The $SMD_{peak\ data\ rate}$ represents the SMD at the spray core where the droplet count is maximum (averaged over four azimuthal locations along two diametric traverses). Typically, the location of the peak data rate coincides with maximum shear, as also adopted in discussing laser Doppler velocimetry data by Mongia et al. (2001). The measurement locations at every stage are indicated in Fig. 25.

In the present experiments, the simplex spray itself is well atomized with a GSMD of 44 μm . As the simplex spray interacts with the primary air, further improvements in the atomization occur at the spray shear layer at which the SMD_{peak} drops to 37 μm from 48.1 μm in Case 1. Considering the bulk relative velocity ($V_R=9\text{--}25\text{ m/s}$; based on gas velocity and liquid sheet velocity of the simplex spray) and initial average droplet size of the simplex spray (37 μm), it is estimated that $We_g \ll 1$. This shows that the improvements in atomization is not by the secondary atomization and the possible mechanism could be the local variations in circulation intensity as the vortices in the shear layer interact with the droplets. However, in the present experiments, it is not possible to determine the gas Weber number based on the circulation intensity.

Subsequently in Case 3, in the absence of secondary air, the wall filming adversely affects the atomization quality as observed in the drastic rise in GSMD (109 μm). Majority of droplets generated by the simplex spray interaction with the primary air directed towards the prefilmer for wall filming. The wall filming erases most of the improvements gained by the primary air swirl. The rim absorbs all the film effects and the further spray formation mainly depends on the rim thickness at the venturi exit, and its interaction with the counter-rotating shear layer. In Case 4, atomization improves drastically reducing GSMD to 67 μm . The rim breakup/ primary

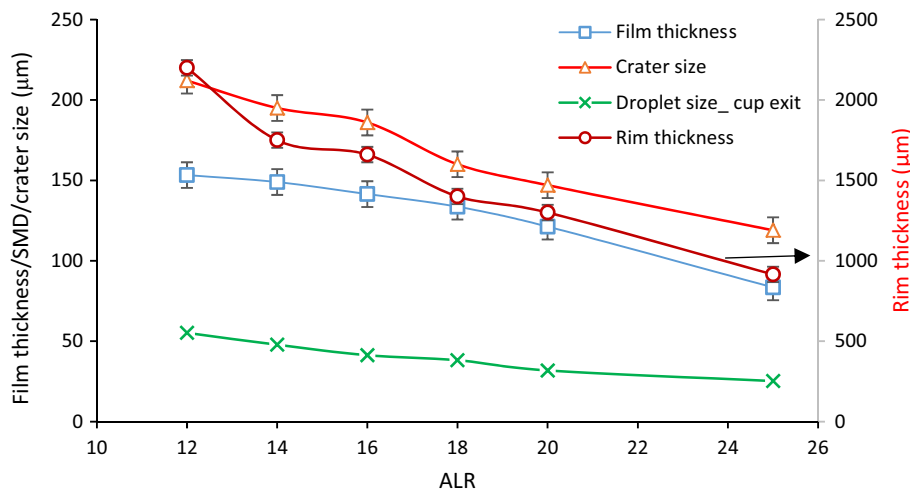
Table 3 GSMD and SMD_{peak} for all cases at an ALR=16

| Test case (locations shown in Fig. 25) | GSMD (μm) | $SMD_{peak\ data\ rate}$ (μm) |
|--|------------------------|--|
| 1. Simplex nozzle ($y/d=0.5$) | 44.16 | 48.9 |
| 2. With primary air ($y/d=0.5$) | 38.60 | 37 |
| 3. At venturi exit ($y/d=1.32$) | 109.89 | 84.5 |
| 4. With secondary swirler ($y/d=1.32$) | 63.37 | 66.5 |
| 5. Full swirl cup ($y/d=1.69$) | 42.04 | 44.2 |
| 6. Full swirl cup ($y/d=1.95$) | 44.07 | 40.5 |
| 7. Full swirl cup ($y/d=2.5$) | 39.38 | 35.5 |
| 8. Full swirl cup ($y/d=3.96$) | 35.83 | 37.55 |

atomization occurs within a very short distance from the prefilmer tip within the shear layer and further atomization is mainly driven by the secondary atomization. The gas velocity at the secondary exit is in the range of 20–42 m/s and the corresponding We_g is in the range of 15–27. At the cup exit, a GSMD of 44.07 μm and a $SMD_{peak\ data\ rate}$ of 40.5 μm are observed. However, between Case 4 and 5, the improvements in GSMD are by the shear layer interaction and droplet redistribution since $We_g < 1$. Further, apart from the GSMD data, the $SMD_{peak\ data\ rate}$ also shows the same trend showing the improvements in atomization.

As compared to the simplex nozzle spray, at the cup exit, a substantial change in droplet size is not observed. Further, GSMD does not indicate improvement in atomization as much as even the $SMD_{peak\ data\ rate}$ across the different configurations tested. This is because the $SMD_{peak\ data\ rate}$ represents the droplet size where the data rate is maximum, which is in the shear layer region. Whereas, the GSMD is averaged over a diametral line in a volume-weighted manner, representing the droplet size of the spray as a whole at

Fig. 24 Variation of measured parameters with ALR



a given axial location, so the local atomizing processes get averaged out.

The above results imply that the individual air streams play a major role as compared to the wall filming process towards improving the atomization in the present atmospheric pressure/room temperature tests with the simplex nozzle. Droplet interaction within the shear layer and successive secondary atomization improve the droplet size in swirl cup, rather than a film breakup based primary atomization. However, in reality, wall filming from a dual orifice nozzle used in the practical swirl cup may be advantageous under high power conditions, particularly in an elevated pressure ambience. In such a case, the fuel flow rates are higher than in the present work, and under rich operating conditions, when the wall filming may be necessary to yield better atomization. Further investigations are required to further validate these details.

3.3 Comparisons with the existing literature

As mentioned in the introduction, a large number studies are reported on prefilming airblast atomization, and most of them presented correlations to predict the mean SMD at the injector exit based on the operating parameters. These correlations depend on operational range, geometry of the injector, measurement location and diagnostic methods. Further, limited studies have performed with practical geometries, and it is important to compare the present work with the existing literature to investigate the applicability of existing models to a practical hardware. In this subsection, the SMD measurements at the swirl cup exit are compared with the existing correlations which are listed in Table 4. A brief summary of these correlations and specific flow conditions can be found in Gepperth et al. (2013).

In terms of overall flow conditions, correlations are selected which match with the present flow conditions at least to a certain extent. In previous investigations, the gas velocity is maintained in the range of 20–120 m/s and

experiments are performed with planar prefilms with various test liquids, e.g., water, kerosene, etc. The exit gas velocity (20–42 m/s) and liquid flow rate (1.15 g/s) in the present experiments are also comparable with the previous investigations. However, the major difference is the wall filming on the curved venturi and rim breakup in the presence of counter-rotating air swirl.

The different terms are listed as follows: m_l and m_g are the liquid and gas flow rates, μ_g and μ_l are the gas and liquid viscosities, σ is the surface tension of water, t is the film thickness, \bar{u}_g is the bulk gas velocity, δ is the boundary layer thickness, and We_δ is the Weber number based on δ . Based on the above, the predicted values are listed in Table 5, with the correlation numbers in different columns corresponding to Table 4. The predicted data sets that match reasonably well with the measurements are plotted in Fig. 26a and the relative error between measurements and predictions are plotted in Fig. 26b. Relative error is estimated as,

$$\% \text{ error} = \frac{\text{SMD}_{\text{corr}} - \text{SMD}_{\text{meas}}}{\text{SMD}_{\text{meas}}}$$

Lefebvre (1980) presented one of the most general correlations [1], and in the present case, the liquid rim thickness is taken as the linear scale L_c . This correlation agrees with the experiments and the error is within 55% for the present test range. Correlations [2], [3], and [4] are based on the experiments with planar atomizers and in the present case maximum film thickness value is taken as t and venturi throat diameter is taken as d_p . The predictions deviate considerably from the measurements and in these cases, and the relative error is even above 500%. The reason for these deviations could be the non-swirling air flows through the planar prefilms, which do not involve considerable shear at the prefilmer tip. Further, this also substantiates that the film thickness has not much role in deciding the final droplet size. Experiments conducted by Sattlemayer and Wittig (1986) on planar prefilmer highlighted the role of prefilmer thickness, but its effect is not included in the correlation [5], which only considers the gas velocity and surface tension. In this case too, measurements do not match well with the predictions.

Correlation [6] is based on the investigations conducted by Aigner and Wittig (1988) with a coaxial swirl injector. They did not observe any effect of the atomizer edge thickness on the final droplet size, as long as the accumulated liquid rim was not affecting the air flow near the prefilmer tip. Interestingly, their correlation matches well with the present experimental data, even though the effect of liquid rim thickness is not considered in their investigation. The relative error is <5% in this case. This shows the additional importance of the secondary atomization since in both present case and the above investigation, the measurement locations are farther downstream from the atomizer edge, and secondary

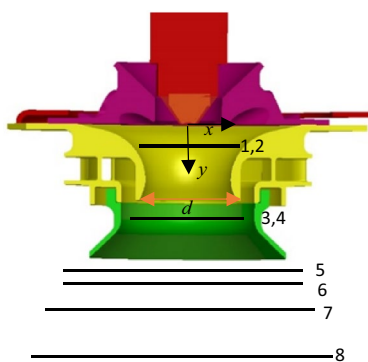


Fig. 25 Schematic of the swirl cup showing the locations of GSMD measurements in Table 3

atomization by the shear layer interactions affects the droplet size considerably.

Geperth et al.’s correlation [7] is based on the measurements that were performed on a planer prefilmer, and measurement location is close to the edge such that the droplets formed by the primary atomization are captured. As a result, the correlation predicts bigger droplets and relative error is > 1000% in some cases. In the present case, the measurement location is away from the venturi tip, and the secondary atomization in the shear layer influences the drop breakup. Further, rather than the prefilmer thickness, the rim size is the most dependent parameter, which is a function of ALR or gas velocity, liquid flow rate, the strength of the swirl shear layer, apart from the edge thickness. It is also important to note that even though the prefilmer thickness and gas velocities in Geperth et al.’s work are comparable to the present experiments, the measured droplet size is at least an order of magnitude higher than that in the present case. This further highlights the importance of the swirl shear layer in improving the atomization.

Correlation [8] is developed by Shanmugas and Chakravarthy (2017) based on the experiments with a coaxial prefilming airblast atomizer, in which a counter-rotating swirler arrangement is used to atomize the liquid rim. This correlation agrees with the measurements, and the error is within 16%. Further, even at lower gas velocities (7–10 m/s), the shear layer efficiently atomizes fairly big rims (1000–4000 μm) to droplet sizes of 109 μm as seen by the above authors. This altogether highlights the importance of the counter-rotating swirler arrangement and the shear layer in improving atomization.

Further, we have also compared a secondary atomization model by Hsiang and Faeth (1992) with the present data. The rim thickness is considered as the initial diameter, and We_g is estimated based on the bulk gas velocity. K is taken as 1.1 based on the experimental data. The predicted values are in good agreement with the measurements with a relative error < 8% of the present test range. This shows the relative importance of secondary atomization in the droplet formation process in swirl cup.

Table 4 Correlations to predict SMD from previous investigations

| | | |
|---|---|-----------------------------------|
| 1 | $\frac{SMD}{LC} = A \left(\frac{\sigma}{\rho_g U_g^2 D_p} \right)^{0.5} \cdot (1 + \dot{m}_l / \dot{m}_g) + B \left(\frac{\mu_l^2}{\sigma \rho_l D_p} \right)^{0.5} \cdot (1 + \dot{m}_l / \dot{m}_g)$ | Lefebvre (1980) |
| 2 | $SMD = 3.33 \times 10^{-3} \frac{(\sigma \rho_l t)^{0.5}}{\rho_g \bar{U}_g} \cdot (1 + 1/ALR) + 13.0 \times 10^{-3} \left(\frac{\mu_l^2}{\sigma \rho_l} \right)^{0.425} \cdot t^{0.575} \cdot (1 + 1/ALR)^2$ | Rizkalla and Lefebvre (1975) |
| 3 | $SMD = 0.073 \left(\frac{\sigma}{\rho_g \bar{U}_g^2} \right)^{0.6} \cdot \left(\frac{\rho_l}{\rho_g} \right)^{0.1} \cdot D_p^{0.4} \cdot (1 + \dot{m}_l / \dot{m}_g) + 0.015 \left(\frac{\mu_l^2 D_p}{\sigma \rho_l} \right)^{0.5} \cdot (1 + \dot{m}_l / \dot{m}_g)$ | Shanawany and Lefebvre (1980) |
| 4 | $SMD = \frac{3}{1/t + (0.00175 \cdot \sigma \bar{u}_g^2 / \rho \cdot (1 + \frac{1}{\dot{m}_g / \dot{m}_l}))}$ | Lefebvre (1992) |
| 5 | $SMD = 0.67 \cdot \frac{\sigma^{0.75}}{\bar{u}_g^{1.57}}$ | Sattelmayer and Wittig (1986) |
| 6 | $SMD \propto \sigma^{0.5} \cdot \rho_g^{-0.4} \cdot \bar{u}_g^{-1.05} \delta^{0.3} \cdot \left(\frac{\dot{m}_l}{\rho_l} \right)^{0.15} \cdot \mu_g^{0.15}$ | Aigner and Wittig (1988) |
| 7 | $\frac{SMD}{\delta_{s_edge}} = 4.96 \cdot \left(\frac{\rho_g \bar{u}_g \delta_{s_edge}}{\mu_g} \right)^{-0.17} \cdot \left(\frac{\rho_g \bar{u}_g^2 \delta_{s_edge}}{\sigma} \right)^{-0.36} \cdot \left(\frac{\rho_l}{\rho_g} \right)^{-0.013} \cdot \left(\frac{h}{\delta} \right)^{0.46}$ | Geperth et al. (2013) |
| 8 | $\frac{SMD}{\delta} = 0.07 We_\delta^{-0.33} (1 + 1/ALR)^{-4.772} \left(\frac{t_{rim}}{\delta} \right)^{0.221}$ | Shanmugas and Chakravarthy (2017) |
| 9 | $\frac{\rho_g SMD \bar{u}_g^2}{\sigma} = k \left(\frac{\rho_l}{\rho_g} \right)^{0.25} \sqrt{\frac{\mu_l}{\rho_l \bar{u}_g D_0}} We$ | Hsiang and Faeth (1992) |

Table 5 Measured and predicted SMD values for different correlations

| ALR | SMD_ measured (μm) | [1] | [2] | [3] | [4] | [5] | [6] | [7] | [8] | [9] |
|------|--------------------|------|------|-------|-------|-------|------|-------|------|------|
| 12.0 | 55.2 | 57.5 | 17.0 | 162.9 | 180.2 | 816.1 | 58.4 | 701.7 | 49.9 | 57.2 |
| 14.0 | 47.8 | 38.8 | 14.1 | 132.9 | 144.9 | 640.7 | 49.4 | 611.6 | 44.7 | 47.2 |
| 16.0 | 41.3 | 31.9 | 12.1 | 113.2 | 118.9 | 519.5 | 42.7 | 543.0 | 41.7 | 43.0 |
| 18.0 | 38.2 | 23.8 | 10.3 | 97.7 | 98.1 | 431.8 | 37.5 | 488.9 | 38.1 | 37.3 |
| 20.0 | 31.8 | 19.8 | 9.0 | 85.6 | 82.5 | 366.0 | 33.4 | 445.1 | 35.6 | 34.1 |
| 25.0 | 25.2 | 11.0 | 7.0 | 64.9 | 56.6 | 257.8 | 26.2 | 364.8 | 29.3 | 25.6 |

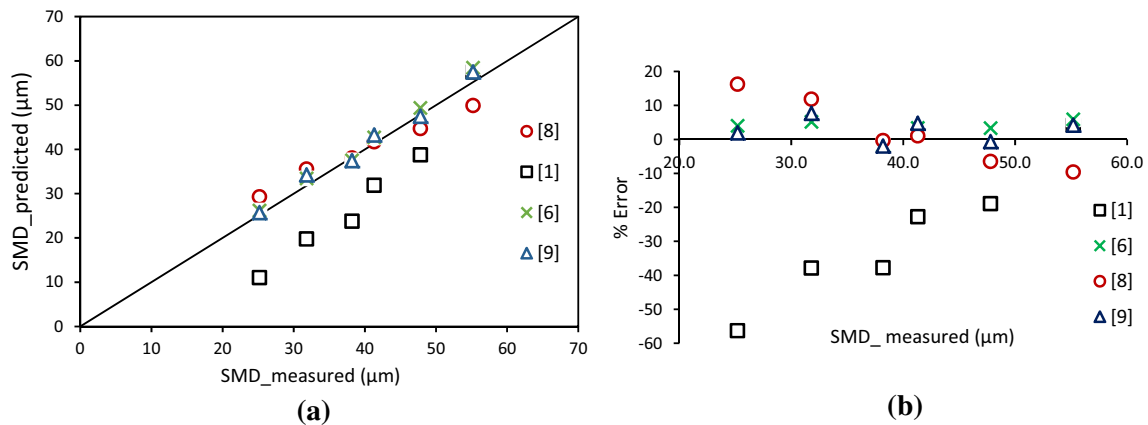


Fig. 26 **a** Comparison between the present measurements and predictive correlations, **b** relative error between predictions and the measurements

3.4 Unsteady flow processes inside swirl cup

In this subsection, the unsteady behaviour of the swirl cup spray is discussed. Even though the mean flow field appears to be axisymmetric, the unsteady flow field reveals a precessing motion of the primary spray. The entire spray cone precesses about the injector axis, as observed in the high-speed images obtained from an oblique view of Case 3 (Fig. 27). This is further verified with the images obtained with the configuration of Case 2 (Fig. 6). The spray precession is driven by the PVC generated by the primary swirl air flow. Wang et al. (2007) observed the existence of the PVC of this air flow in the swirl cup at similar flow conditions in their LES. In their study, the PVC frequency is estimated as 1277 Hz. In the present case, the spray precession frequency is estimated as 1002 Hz by Fourier transform of the Mie scattering intensity at a point (marked in Fig. 27) near the injector tip in Case 3; the spectrum is shown in Fig. 28a. The lower frequency observed in the present case could be due to the injection of the droplets into the primary air swirl flow field, which dampens the strength of the PVC and causes it to precess more slowly than that of the single phase air swirl. The direction of precession of the PVC is observed to be the same as that of the primary swirl air flow.

The precessing motion of the flow passing through the convergent–divergent passage of the venturi causes the spray to impinge on the venturi wall in a periodic and non-axisymmetric manner. This results in an azimuthally non-uniform film thickness along the venturi.

The droplet impingement frequency on the venturi wall is estimated as 934 Hz by the Fourier transform of the LIF intensity from the LDM–PLIF images (Fig. 12). The corresponding spectrum is shown in Fig. 28b. This periodic droplet impingement causes film thickness fluctuations, which are, however, found to be aperiodic, as seen below.

The spectrum of the film thickness fluctuations corresponding to the impinging location is shown in Fig. 28c. It can be noted that there exists many different frequencies related to the film thickness fluctuations. However, a predominant peak of 851 Hz can be observed, which is lesser than the droplet impingement frequency. The film thickness fluctuation frequency could be influenced by the impingement process in several ways: apart from the periodic droplet impingement, the film thickness fluctuations are further affected by the impinging droplet size, impinging angle, splashing or deposition, shearing of the film by the primary air flow to form new droplets, etc.

The spectra of the ligament and droplet shedding at the venturi tip are obtained from the LIF intensity signals taken at different regions as marked in Fig. 20a. The droplet shedding frequency at the venturi tip is estimated for each case. For this, different regions of the image—near the rim tip (left and right regions), inside the venturi region and the bottom region of the venturi, are selected and analysed. The spectrum for the ALR = 16 case is shown in Fig. 28d. A dominant frequency of 986 Hz is observed, which corresponds to the fine droplet shedding from the film (Figs. 9a, 19a). This is slightly less when compared to the droplet precession frequency of 1002 Hz mentioned above. This shows that the fine droplet shedding frequency matches with that of the droplet impingement and spray precession frequency, which are driven by the PVC of the primary swirl air flow.

However, the ligament shedding at the venturi exit appears to be aperiodic since multiple droplets of varying sizes are produced at the venturi tip and are shed at different rates ranging from 40 to 500 Hz. Thus, the ligament shedding process is unaffected by the PVC. The ligaments originate from the accumulated rim and their shedding is mainly influenced by the rim thickness and the shear layer surrounding the venturi tip. Further, the time taken for the

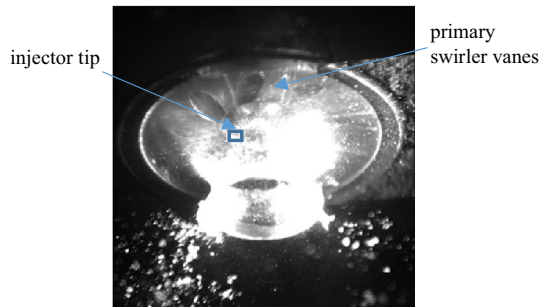


Fig. 27 Oblique view image of the Case 3 configuration showing the injector tip

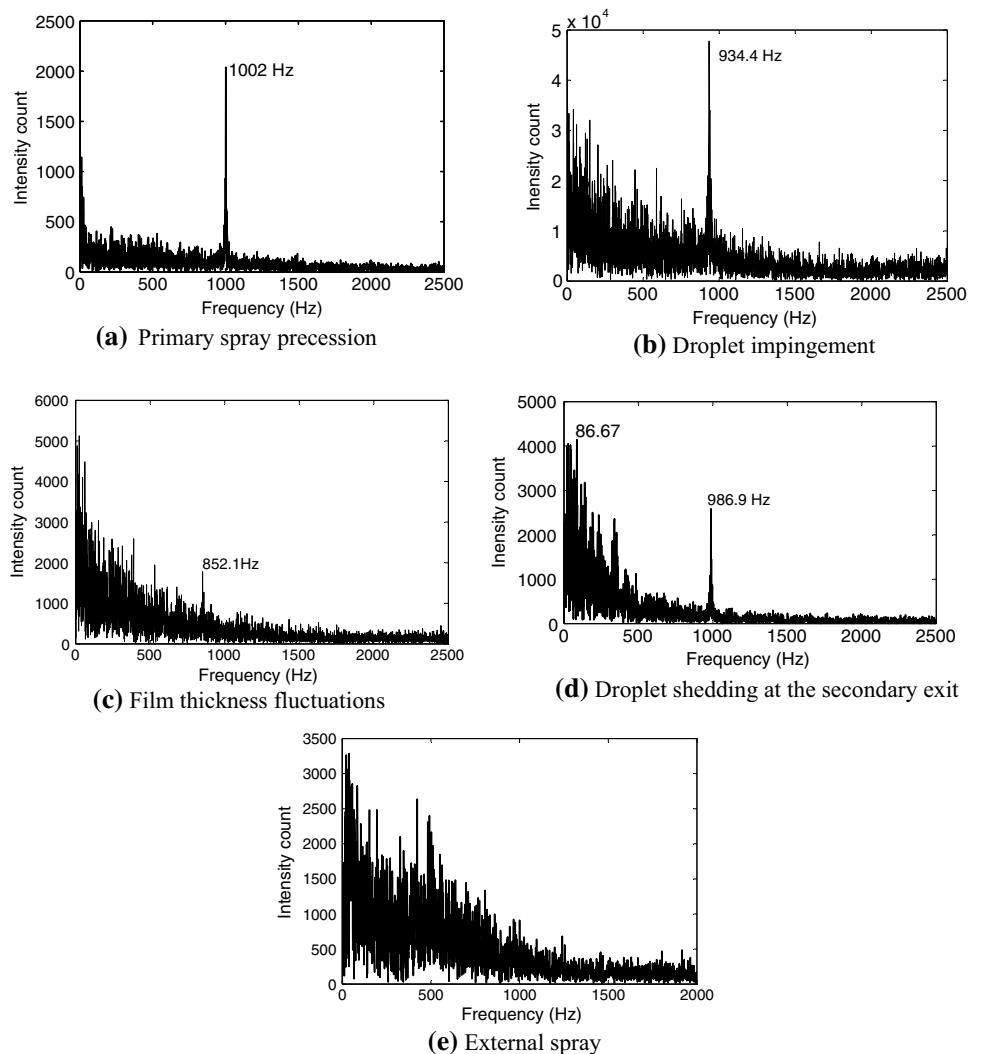
spiralling motion of the film to reach the tip and the accumulation time of the liquid rim are much greater than the precession time scale.

At the swirl cup exit too, the spray behaviour is largely unaffected by the PVC, as seen in the spectrum of the

intensity fluctuations from the droplets exiting the swirl cup along the shear layer (Fig. 28e). It involves a wide range of frequencies that are mainly related to the ligament shedding. This is because, most of the droplets at the swirl cup exit originate from secondary atomization of ligaments of a wide size range formed at the venturi tip, and their formation is not influenced by the PVC, as seen above. In any case, the fine droplets mix in the shear layer, so their periodic shedding observed at the venturi tip does not carry through at the swirl cup exit.

As expected, increase in the ALR results in the increase in the primary swirl PVC frequency, and consequently, the frequencies of precession, impingement, and droplet shedding increase. The variation of these frequencies with ALR is shown in Fig. 29. The frequencies match quite well at low ALR but diverge slightly as the ALR is increased. This is due to the accumulation of the liquid rim and the mixing of the fine droplets shed at the venturi tip, which are amplified as the air flow rate is increased.

Fig. 28 Frequency spectra of different flow processes at ALR 16



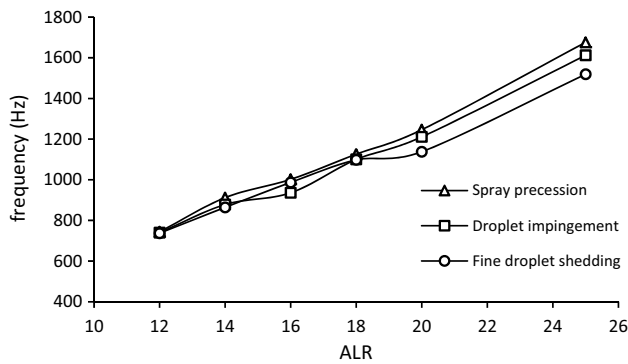


Fig. 29 Variation of the spray precession, impingement, and fine droplet shedding frequencies with ALR

4 Conclusions

The present work investigates various internal atomization processes of a practical gas turbine fuel injector using advanced laser diagnostic techniques. The internal flow field is characterized using different geometrical configurations (five cases) of the swirl cup. Stage-wise PDI and imaging experiments are performed systematically to assess the spray behaviour, as the atomization evolves through the swirl cup. The internal two-phase flow field of the swirl cup is captured by TR-VLIF experiments in a range of imaging configurations. The flow field inside the venturi is visualized using a transparent hardware to understand the overall flow field. Considering the microscopic nature of the phenomena involved, a high-resolution TR-PLIF imaging is adopted with the help of the long distance microscope to investigate the film behaviour.

The droplet size and velocity distribution data are used to understand the role of individual swirl cup components on improving the atomization and the flow field. Stage-wise characterization shows that the atomization process is mainly improved by the individual air streams. The initial interaction is between the simplex spray and the primary air. The spray structure mainly evolves with the CTRZ and the shear layer helps in improving the atomization and mixing. The primary spray impinges on the venturi prefilmer, which results in splashing and deposition on the liquid film along its walls. The combined action of the spray impingement and the shearing by the primary swirling air makes the wall filming process highly dynamic. The liquid flowing along the film accumulates into a rim at the venturi tip, where it interacts with the shear layer between the counter-rotating primary and secondary swirl air flows at the venturi tip. This shear layer helps on the formation of thinner liquid rim uniformly distributed around the venturi tip and a clustered

ligament shedding at multiple azimuthal locations around the prefilmer.

The unsteady spray behaviour inside the swirl cup is mainly driven by the PVC associated with the primary swirl. The precessing motion of the primary spray controls subsequent processes such as periodic droplet impingement, circumferential film oscillations, spiral film shearing/ finer droplet shedding. However, the ligament breakup and successive atomization process and the external spray are unaffected by the PVC.

In the present work, the crater formation is captured by the LDM-PLIF imaging, and the process is quantified to obtain its size distribution. The film and the rim thicknesses are quantified for different operating conditions. Besides, the various dominant frequencies of periodic spray precession, impingement on the venturi wall, film thickness oscillations, and droplet shedding at the venturi exit are quantified as well. The thick liquid rim formed at the venturi tip is identified as the major source of droplets and the main deciding factor of the SMD at the swirl cup exit.

The atomization mechanism alters as the spray evolves through the cup at every stage. The initial GSMD improvements are obscured by the venturi wall filming and further improvements in GSMD are contributed by the shear layer and successive secondary atomization. Therefore, the atomization process is mainly driven by the shear layer and secondary atomization rather than the film dynamics or primary breakup process, unlike what is focused upon in the previous literature. Further, in the present work, the measured SMD at the swirl cup exit is compared with the correlations based on generic configurations in the literature. Correlations highlighting the role of secondary atomization and liquid rim thickness are found to agree well with the measurements.

The present study provides a detailed and comprehensive characterization explaining the atomization physics in a practical gas turbine injector, capturing the internal mechanisms in detail. This provides insights into the complicated processes occurring in a real geometry. The understanding and the measurements reported here can be utilized in improving prefilming airblast atomizers and to validate computational simulations of the underlying processes.

Acknowledgements We acknowledge GE India Industrial PVT. LTD., Bengaluru for the financial support and for providing the nozzle hardware. The National Centre for Combustion R&D is supported by the Science and Engineering Research Board, India.

References

Aigner M, Wittig S (1988) Swirl and counterswirl effects in prefilming airblast atomizers. *J Eng Gas Turb Power* 110(1):105–110

- Bachalo WD, Houser MJ (1984) Phase/doppler spray analyzer for simultaneous measurements of drop size and velocity distributions. *Opt Eng* 23(5):235583
- Barun S, Weith L, Koch R, Bauer H-J (2015) Influence of trailing edge height on primary atomization: numerical studies applying the smoothed particle hydrodynamics (SPH) method. In: 13th Triennial international conference on liquid atomization and spray systems, Taiwan
- Batarseh FZ (2008) Spray generated by an airblast atomizer: atomization, propagation and aerodynamic instability. PhD Thesis, TU Darmstadt
- Batarseh FZ, GnirB M, Roisman IV, Tropea C (2009) Fluctuations of a spray generated by an airblast atomizer. *Exp Fluids* 46:1081–1091
- Bhayaraju U, Hassa C (2009) Planar liquid sheet breakup of prefilming and non-prefilming atomizers at elevated pressures. *Atomization Sprays* 19:1147–1169
- Brundish KD, Miller MN, Morgan LC, Wheatley AJ (2003) Variable fuel placement injector development. In: ASME Turbo Expo 2003, Atlanta, Georgia, USA, GT2003-38717
- Cai J, Fu Y, Elkady A, Jeng S, Mongia HC (2003) Swirl cup modelling part 4: effect of confinement on flow characteristics. In: 41st AIAA aerospace sciences meeting and exhibit, Reno, Nevada, AIAA Paper 2003-486
- Elshanawany MS, Lefebvre AH (1980) Airblast atomization—effect of linear scale on mean drop size. *J Energy* (4):184–189
- Foust M, Thomsen D, Stickles R, Cooper C, Dodds W (2012) Development of the GE Aviation low emissions TAPS combustor for next-generation aircraft Engines. In: 50th AIAA aerospace sciences meeting, Nashville, Tennessee, USA, AIAA paper 2012-936
- Gepperth S, Guildenbecher D, Koch R, Bauer H-J (2010) Prefilming primary atomization: experiments and modelling. In: 23rd Annual conference on liquid atomization and spray systems, ILASS Europe, Brno, Czech Republic
- Gepperth S, Muller A, Koch R, Bauer H-J (2012) Ligament and droplet characteristics in prefilming airblast atomization. In: 12th Triennial international conference on liquid atomization and spray systems, ICLASS 2012, Heidelberg, Germany
- Gepperth S, Koch R, Bauer H-J (2013) Analysis and comparison of primary droplet characteristics in the near field of a prefilming airblast atomizer. In: ASME. Turbo Expo: Power for Land, Sea, and Air, Volume 1A: Combustion, Fuels and Emissions, pp V01AT04A002
- Gupta AK (1997) Gas turbine combustion: prospects and challenges. *Energy Convers Manag* 38:1311–1318
- Gupta AK, Lilley DG, Syred N (1984) Swirl flows. Abacus Press, Tunbridge Wells
- Gurubaran K, Chakravarthy SR, Sujith RI (2008) Characterization of a prefilming airblast atomizer in a strong swirl flow field. *J Propul Power* 24:1124–1132
- Hsiang L-P, Faeth GM (1992) Near-limit drop deformation and secondary breakup. *Int J Multiph Flow* 18(5):635–652
- Hsiao G, Mongia HC (2003) Swirl cup modelling part III: Grid independent solution with different Turbulence Models. In: 41st AIAA aerospace sciences meeting and exhibit, Reno, Nevada, AIAA Paper 2003-1349
- Huang Y, Yang V (2009) Dynamics and stability of lean-premixed swirl-stabilized combustion. *Prog Energy Combust Sci* 35:293–364
- Inamura T, Shiota M, Tsushima M, Kato M, Hamajima S, Sato A (2012) Spray characteristics of prefilming type of airblast atomizer. In: 12th Triennial international conference on liquid atomization and spray systems, ICLASS 2012, Heidelberg, Germany
- Jasuja AK (2006) Behaviour of aero-engine airblast sprays in practical environments. In: 10th Triennial international conference on liquid atomization and spray systems, ICLASS 2006, Kyoto, Japan
- Jeng S-M, Flohre N, Mongia HC (2004) Swirl Cup Modeling-part IX: liquid atomization modelling. In: 42nd AIAA aerospace sciences meeting and exhibit, Reno, Nevada, USA, AIAA Paper 2004-137
- Lefebvre AH (1975) Pollution control in continuous combustion engines. 15th Symp (Int) Combust 15(1):1169–1180
- Lefebvre AH (1980) Airblast atomization. *Prog Energy Combust Sci* 6:233–261
- Lefebvre AH (1992) Twin-fluid atomization: Factors influencing mean drop size. *Atomization Sprays* 2:101–119
- Lin Y, Lin Yu, Liu G (2009) Unsteady flow structures of a counter-rotating swirl cup. In: 45th AIAA/ASME/SAE/ASEE joint propulsion conference and exhibit, Denver, Colorado, USA, AIAA paper 2009-2016
- McDonell VG, Seay JE, Samuelsen S (1994) Characterization of the non-reacting two-phase flow downstream of an aero-engine combustor dome operating at realistic conditions In: ASME International gas turbine and aero-engine congress and exposition, Hague, Netherlands, ASME Paper 1994- GT-263
- Mongia HC, Al-Roub M, Danis A, Elliott-Lewis D, Jeng S, Johnson A, McDonell V, Samuelsen G, Vise S (2001) Swirl cup modelling part 1. In: 37th joint propulsion conference and exhibit, Salt Lake City, UT, USA, AIAA Paper 2001-3576
- Rajamanickam K, Basu S (2017a) On the dynamics of vortex—droplet interactions, dispersion and breakup in a coaxial swirling flow. *J Fluid Mech* 827:572–613
- Rajamanickam K, Basu S (2017b) Insights into the dynamics of spray—swirl interactions. *J Fluid Mech* 810:82–126
- Rizk NK, Lefebvre AH (1980) The Influence of liquid-film thickness on airblast atomization. *J Eng Power* 102(3):706–710
- Rizk NK, Lefebvre AH (1983) Spray characteristics of plain-jet airblast atomizers. *J Eng Gas Turbines Power* 106(3):634–638
- Rizkalla AA, Lefebvre AH (1975) The Influence of air and liquid properties on airblast atomization. *J Fluids Eng* 97(3):316–320
- Rodríguez DJ, Shedd TA (2004) Entrainment of gas in the liquid film of horizontal annular two-phase flow. *Int J Multiph Flow* 30(6):565–583
- Roisman IV, Tropea C (2002) Impact of a drop onto a wetted wall: description of crown formation and propagation. *J Fluid Mech* 472:373–397
- Roisman IV, Tropea C (2005) Fluctuating flow in a liquid layer and secondary spray created by an impacting spray. *Int J Multiph Flow* 31(2):179–200
- Roisman IV, Hinsberg NP, Tropea C (2008) Propagation of a kinematic instability in a liquid layer: capillary and gravity effects. *Phys Rev E* 77:046305
- Sattelmayer T, Wittig S (1986) Internal flow effects in prefilming airblast atomizers—mechanisms of atomization and droplet spectra. *J Eng Gas Turb Power* 108:465–472
- Schildmacher KU, Koch R, Wittig S, Krebs W, Hoffmann S (2000) Experimental investigations of the temporal air-fuel mixing fluctuations and cold flow instabilities of a premixing gas turbine burner. In: ASME Turbo Expo 2000: power for land, sea, and air. Munich, Germany, ASME Paper 2000-GT-0084
- Schubring D, Ashwood AC, Shedd TA, Hurlburt ET (2010) Planar laser-induced fluorescence (PLIF) measurements of liquid film thickness in annular flow Part I: methods and data. *Int J Multiph Flow* 36(10):815–824
- Shanmugasdas KP, Chakravarthy SR (2017) A canonical geometry to study wall filming and atomization in prefilming coaxial swirl injectors. *Proc Combust Inst* 36(2):2467–2474
- Sivakumar D, Tropea C (2002) Splashing impact of a spray onto a liquid film. *Phys Fluids* 14:L85
- Syred N (2006) A review of oscillation mechanisms and the role of the precessing vortex core (PVC) in swirl combustion systems. *Prog Energy Combust Sci* 32:93–161

- Syred N, Beer JM (1974) Combustion in swirling flows: a review. *Combust Flame* 23(2):143–201
- Wang HY, McDonnell VG, Samuelsen GS (1992) The two-phase flow downstream of a production engine combustor swirl cup. *Symp (Int) Combust* 24(1):1457–1463
- Wang H, McDonnell VG, Sows WA, Samuelsen S (1994) Experimental study of a model gas turbine combustor swirl cup, Part 11: droplet dynamics. *J Propul Power* 10:446–452
- Wang HY, McDonnell VG, Samuelsen GS (1995) Influence of hardware design on the flow field structures and the patterns of droplet dispersion: Part I—mean quantities. *J Eng Gas Turbine Power* 117:282–289
- Wang SW, Yang V, Hsia G, Hsieh SY, Mongia HC (2007) Large-eddy simulations of gas-turbine swirl injector flow dynamics. *J Fluid Mech* 583:99–122

Publisher's Note Springer Nature remains neutral with regard to jurisdictional claims in published maps and institutional affiliations.

Affiliations

K. P. Shanmugas¹  · S. R. Chakravarthy¹ · R. Narasimha Chiranthan² · Jayanth Sekar² · Sundar Krishnaswami²

✉ S. R. Chakravarthy
src@ae.iitm.ac.in

² GE India Industrial Pvt. Ltd., Bengaluru, India

¹ Department of Aerospace Engineering, and National Centre for Combustion Research and Development, Indian Institute of Technology Madras, Chennai 600036, India